Technische Universität München
Fakultät für Medizin

Enhancing Brain Tumor Imaging: A Novel Deep Learning-Based Approach for Recurrence Prediction of Glioblastoma

Marie-Christin Metz

Vollständiger Abdruck der von der Fakultät für Medizin der Technischen Universität München zur Erlangung des akademischen Grades einer Doktorin der Medizin genehmigten Dissertation.

Vorsitz:	Prof. Dr. Marcus R. Makowski
Prüfer*innen der Dissertation:	1. Priv.-Doz. Dr. Benedikt Wiestler
	2. Prof. Dr. Stephanie E. Combs

Die Dissertation wurde am 30.08.2021 bei der Technischen Universität München eingereicht und durch die Fakultät für Medizin am 07.12.2021 angenommen.

Abstract

Glioblastoma is the most common primary malignant brain tumor and still carries a bleak prognosis despite intensive treatment. In order to guide more personalized treatment options, a lot of scientific effort has been put into developing means to investigate the peritumoral edema for microscopic tumor infiltration. Diffusion Tensor Imaging (DTI) has emerged as a promising imaging tool for the detection of microstructural tissue alterations. However, its application in the assessment of peritumoral edema is impeded by partial volume effects due to free-water contamination.

The purpose of this thesis was to evaluate a novel deep learning-based approach for correcting the free-water contamination of DTI data for its utility in recurrence prediction of glioblastoma. Therefore, in a first step, in 35 glioblastoma cases from our institute's prospective glioma cohort, semi-automatic tumor segmentation was performed on the preoperative MR images as well as on the first postoperative scans showing tumor recurrence. Subsequently, a novel algorithm for free-water correction (FWC) was applied on the DTI data by employing an artificial neural network that disentangles the free-water and tissue component for each voxel. The resulting tissue volume maps (TVM), as well as fractional anisotropy (FA) and mean diffusivity (MD) values were collected for areas with and without later tumor recurrence in the peritumoral edema.

The results show that FWC FA values are significantly lower in areas of the peritumoral edema where later recurrence occurred, even in the lowest range of FA values (in clear contrast to uncorrected FA data). However, the FWC of MD values seems to bring no benefit to their application in recurrence prediction, which might be explained by the reduction of isotropic diffusion signal through the FWC.

Consequently, FWC is a powerful tool for improved brain tumor imaging with the potential for refining surgical and radiotherapy planning in the near future.

Zusammenfassung

Unter allen primären bösartigen Tumoren des zentralen Nervensystems stellen Glioblastome die mit Abstand häufigste Untergruppe. Leider ist ihre Prognose bis heute infaust und selbst die maximale Therapie an hochspezialisierten Zentralen verbessert die Überlebenszeit für betroffene Patienten nur unwesentlich.

Ein wichtiger Schwerpunkt der Hirntumorforschung ist daher die Weiterentwicklung der MRT-Bildgebung mit dem Ziel, personalisierte Behandlungspläne für die Chirurgie und Strahlentherapie zu erhalten. Ein besonderes Augenmerk liegt dabei auf der Darstellung des Perifokalödems des Tumors, da die überwiegende Mehrheit der Rezidive in diesem Bereich auftritt, die mikroskopische Infiltration von Tumorzellen allerdings in den konventionellen MRT-Sequenzen nicht visualisiert werden kann. Die Diffusions-Tensor-Bildgebung (DTI) und insbesondere die daraus ableitbare Fraktionelle Anisotropie (FA) haben sich als vielversprechende Ansätze für diese Fragestellung herausgestellt. Allerdings sind ihre Werte durch die Kontamination von Wasser im Perifokalödem verzerrt.

Das Ziel dieser Promotionsarbeit ist es deshalb, einen Lösungsansatz vorzustellen, wie man diese Wasserkontamination der DTI-Daten beseitigen und dadurch Gewebeveränderungen durch anderweitig „unsichtbare“ Tumorinfiltration aufdecken kann. Dies wird am Beispiel von 35 Glioblastom-Fällen aus der prospektiven Gliom-Datenbank unseres Institutes dargestellt.

Dafür wird in einem ersten Schritt eine semi-automatische Segmentierungsmethode angewandt, die das Perifokalödem vom Kontrastmittel-anreichernden Tumoranteil abgrenzt. In einem zweiten Schritt werden daraufhin die DTI-Datensätze vom Störfaktor des freien Wassers befreit. Die hierfür entwickelte Methode basiert auf einem neuronalen Netzwerk, welches in jedem Voxel den Anteil freien Wassers bzw. Gewebes schätzt und daraus korrigierte FA-Werte generieren kann (neben korrigierten Werten der Allgemeinen Diffusivität (MD) und eigens entwickelten Gewebevolumen-Karten).

Ein Vergleich zwischen den unkorrigierten und den korrigierten DTI-Daten zeigt, dass die korrigierten FA-Werte in Bereichen des Perifokalödems, in denen später das Rezidiv auftritt, bereits in den präoperativen MRT-Bildern signifikant verändert sind. Im Gegensatz dazu ergibt eine Analyse der korrigierten MD-Werte und der Gewebevolumen-Karten keinen zusätzlichen Nutzen.

Die hier vorgestellte Methode könnte in Zukunft dabei helfen, die Lokalisation von späteren Tumorrezidiven bereits auf den ersten präoperativen MRT-Bildern vorherzusagen. Dadurch könnte die chirurgische und strahlentherapeutische Behandlung von Glioblastomen präzisiert

werden, um dadurch einen erheblich verbesserten Therapieerfolg für betroffene Patienten zu gewährleisten.

CONTENTS

1. Motivation and Outline

1.1 Motivation

Glioblastoma (GBM, historically for *glioblastoma multiforme*) is the most common, and at the same time, the most aggressive primary brain tumor. Despite intensive treatment efforts, the median overall survival (MOS) only reaches 15.6 months [1]. Unfortunately, after initial therapy (which usually consists of surgical resection and combined radiochemotherapy) recurrence occurs in essentially all patients with a progressive-free survival (PFS) of only 6 to 9 months [2]. One of the most fatal biological characteristics of GBM leading to this bleak prognosis is their ability to diffusely infiltrate the surrounding brain tissue. Since it is a commonly accepted assumption that the contrast enhancing tumor margins on Magnetic Resonance Imaging (MRI) do not represent the true tumor borders, major scientific efforts are dedicated for developing means to assess more accurately the peritumoral edema for microscopic tumor infiltration. Importantly, 90% of tumor recurrences develop within the peritumoral edema [3], an area that is especially difficult to examine because of the large partial volume effects of free water. Particularly *diffusion tensor imaging* (DTI), an imaging method that enables the visualization of tissue microstructure, is impeded by the water component of the peritumoral edema, which is why studies assessing its utilization for recurrence prediction have shown contradictory results [4]. However, in 2009, Pasternak et al. introduced an algorithm that extracts the free-water component from diffusion MRI enabling a better estimation of tissue-specific indices [5], such as *fractional anisotropy* (FA) which reflects the directionality of brain fiber tracts and has shown to correlate with cell density and proliferation activity [6].

The purpose of this project was to substantially advance this promising approach and, in a next step, evaluate its applicability for recurrence prediction in GBM patients. For that, our team developed a novel method of free-water elimination based on the implementation of an *artificial neural network* (ANN) that can be retrospectively applied to any diffusion MRI data [7].

Our main goal was to obtain valuable image information for personalized treatment decisions which might eventually lead to improved survival times for GBM patients in the future.

1.2 Outline

This thesis begins with a profound introduction to the theoretical background of the project. The first section focuses on DTI, the central MRI modality used in this work (*Section 2.1*).

Next, I provide an overview of the current state of clinical management of GBM and its medical background (*Section 2.2*). This is followed by a chapter dedicated to the well-established imaging protocol of GBM as well as the latest advancements in brain tumor imaging and is subdivided into the preoperative and the postoperative assessment (*Section 2.3*).

The main part describes our research project in detail, including a detailed protocol of the methodology (*Section 3*), the presentation of the results (*Section 4*), and a comprehensive discussion of the results with regard to the current state of the relevant research (*Section 5*). The thesis is concluded with a short summery and an outlook on future research options (*Section 6*).

2 Theoretical Background

This section aims to provide the reader with a solid understanding of the theoretical prerequisites of this thesis. It is divided into three parts: An introduction to DTI (*Section 2.1)* and to the clinical background of GBM (*Section 2.2*), which is concluded with an overview on imaging procedures for GBM (*Section 2.3*).

2.1 Diffusion Tensor Imaging

DTI is an enhancement of the classical *diffusion weighted imaging* (DWI), which is useful for addressing specific questions as those outlined in this project, dealing with the detection of alterations in tissue microstructure. In fact, DTI is a specific type of modeling DWI. Therefore, I start with briefly explaining the background of DWI.

2.1.1 Diffusion Weighted Imaging

In principle, DWI measures the *Brownian motion*, i.e., the random molecular movement of water molecules [8]. In the human body, an uninhibited pattern of such motion is only present within "pure" body fluids, like cerebrospinal fluid (CSF). In most tissues, for example in brain matter, various cellular, subcellular, and extracellular structures impede the movement of water molecules. Therefore, the "velocity" of diffusion is lower in tissue. This velocity is referred to as *diffusion* (D). Since it is impossible to exactly measure D, the corresponding value in MR imaging is referred to as the *apparent diffusion coefficient* (ADC).
To make an MR image sensitive to diffusion, typically a pair of gradient pulses is applied at very high amplitude, one before and one after the 180° radiofrequency pulse. Usually, ultrafast *echoplanar imaging* (EPI) acquisitions are used so that the small-scale motion due to diffusion is not overwhelmed by larger-scale physiologic or gross patient motion [9]. The term *b-value* is used to describe the net gradient effect and therefore, the total amount of diffusion sensitization:

$$b - value = \gamma^2 G^2 \delta^2 (\Delta - \delta/3)$$

It is determined by the *gyromagnetic ratio γ,* the *gradient strength G*, the time the gradients

are kept on (δ), and the time interval between the two pulsed gradients (Δ). Its unit is [s/mm^2][10]. Typically, *b-values* of 700 to 1000 are used in clinical DWI. To generate an image

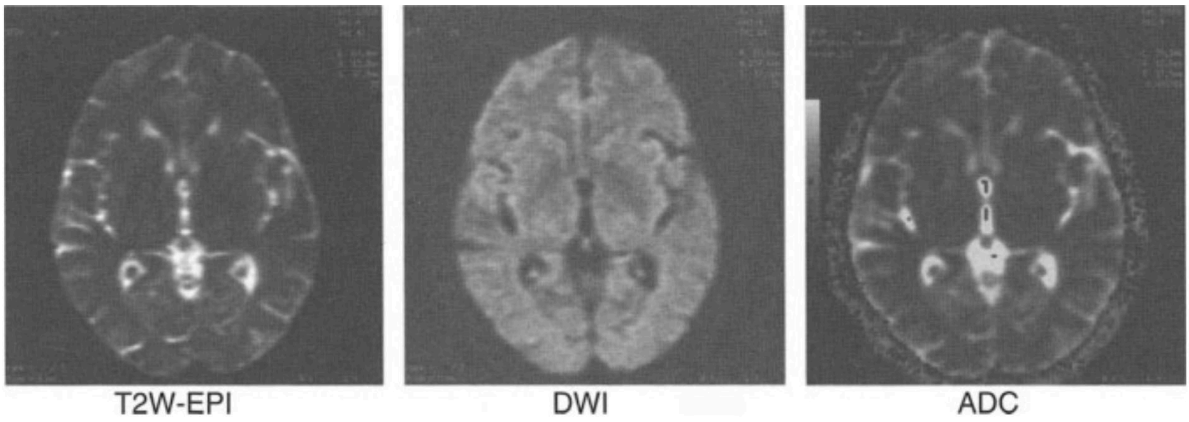

Figure 1 *- Diffusion Weighted Imaging. On the left, there is a T2-weighted EPI image without any diffusion-sensitizing gradient (the b=0 image). On the image in the middle, a diffusion-sensitizing gradient is added making the ventricles appear dark because of signal loss due to diffusion of spins in CSF (DWI). On the right, there is the calculated ADC map that quantifies the magnitude of diffusion as described in the text* [11].

that is sensitive to diffusion in all directions, three orthogonal diffusion-sensitizing gradients are applied subsequently. In single-shot imaging techniques like EPI, T1 contrast is naturally not present. Thus, DWI generally employs T2-weighted EPI images. A routine DWI study consists of the acquisition of four sets of T2-weighted EPI images: One without any diffusion sensitization (the *b=0* image) and three with the addition of diffusion-sensitizing gradients (the diffusion-weighted images, e.g., *b=1000*).

Given the T2-weighted nature of these images, a quantitative measurement of diffusion is necessary to distinguish areas with high T2 signal (e.g., due to edema) from areas with true diffusion restriction. To approximate this ADC, a two-point method is sufficient: When plotting the signal intensity from the *b=0* image and that from the *b=1000* images, the slope of the resultant line will approximate the ADC. As a result, regions with abnormally restricted diffusion will appear with high signal on the DWI and a relatively low pixel intensity (not signal intensity because it is a calculation) on the ADC map. In contrast, areas with high T2 signal but without restricted diffusion will not appear dark on the ADC map (see *Figure 1*) [11].

2.1.2 Diffusion Tensor Imaging

The development of DTI was a major achievement in the field of white matter mapping. It has been introduced by Basser et al. in 1994 [12]. Whereas DWI only measures the magnitude of

diffusion, DTI can give directional information about the diffusion in tissue, i.e., the absolute direction of diffusion and the homogeneity of diffusion direction within a voxel.

The basic concept of DTI is that water molecules diffuse differently along tissues depending on the type, integrity and architecture of tissue. In CSF and any other "pure" liquid, diffusion is unrestricted in all directions which is called *isotropic* diffusion. In contrast to that, the diffusion in white matter is not the same in all directions of a three-dimensional space, e.g., it is usually less restricted along the axon. This is called diffusion *anisotropy*. For each voxel, the diffusion direction and its anisotropy can be described using the second-rank *diffusion tensor*, a 3 x 3 symmetric matrix derived from diffusivity measurements in at least six noncollinear directions. It can be visualized as an ellipsoid whose diameter in any direction describes the diffusivity in that direction. The orientation of the long axis of this ellipsoid depicts the preferred direction of diffusion at a given voxel. This is referred to as the *principle eigenvector* and can be described by an *eigenvector* ε (that reflects the direction of diffusion) and its length, the *eigenvalue* λ (which represents the magnitude of diffusion in that direction). Most commonly, three orthogonal vectors (each with an *eigenvector* and an *eigenvalue*) are used for describing the ellipsoid. In CSF, where diffusion is completely random, the ellipsoid will become a sphere, illustrating *isotropy* [11].

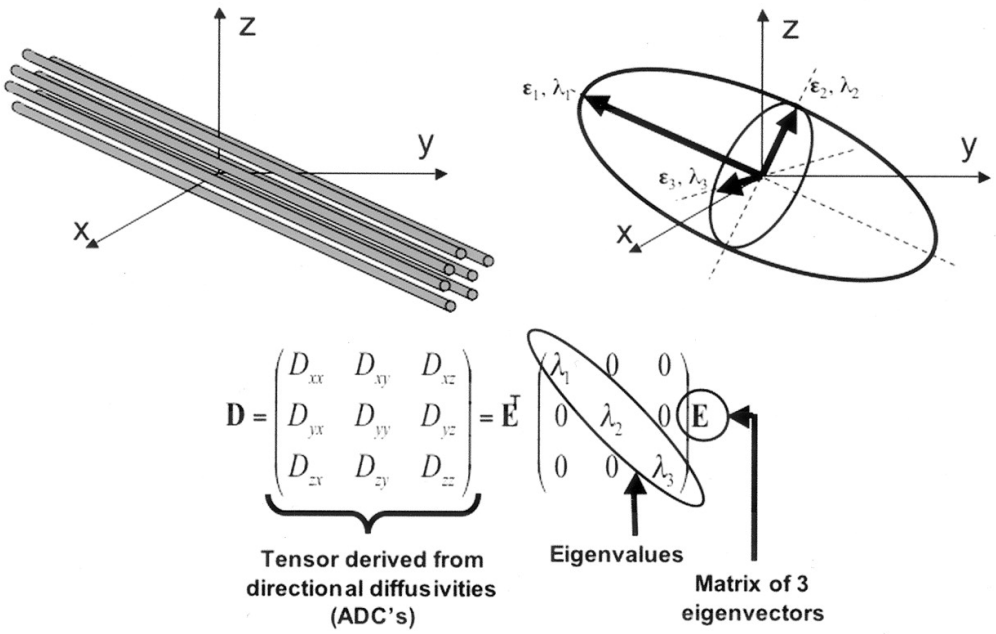

Figure 2 *- Diffusion Tensor Imaging. Top left: Fiber tracts arbitrarily oriented in the xyz-coordinate system of the scanner lead to anisotropic diffusion. Top right: The three-dimensional diffusivity can be modeled as an ellipsoid with three eigenvectors (ε_1, ε_2, ε_3) and their corresponding eigenvalues (λ_1, λ_2, λ_3). Bottom: Via matrix diagonalization the ellipsoid model is fitted to a set of at least six noncollinear diffusion measurements (ADCs). It results in a matrix of three eigenvectors*[13].

The 3 x 3 tensor matrix is *diagonally symmetric* ($\mathbf{D}_{ij} = \mathbf{D}_{ji}$) with six degrees of freedom. This means that only six of the tensor matrix's nine values are independent and thus, the matrix is fully determined by these six parameters [13]. That is the reason why at least six diffusion-encoded measurements are required to fully describe the tensor (see *Figure 2*). However, using more than six encoding directions will improve the accuracy of tensor measurement [14].

Mathematically, diffusion anisotropy can be seen as the degree to which the three tensor eigenvalues differ from each other. The most common metric to describe this is the *fractional anisotropy* (FA). It derives from the standard deviation of the three *eigenvalues* and has a range from 0 (*isotropy*) to 1 (*anisotropy*). The FA can be calculated for each voxel using the following formula:

$$FA = \sqrt{\frac{3}{2}}\sqrt{\frac{(\lambda_1-\bar{\lambda})^2+(\lambda_2-\bar{\lambda})^2+(\lambda_3-\bar{\lambda})^2}{\lambda_1{}^2+\lambda_2{}^2+\lambda_3{}^2}},$$

where $\bar{\lambda}$ denotes the mean of the three eigenvalues, which is equal to the directionally averaged diffusivity of each voxel [$\bar{\lambda} = (\lambda_1 + \lambda_2 + \lambda_3) / 3$]. FA itself has no information about the orientation. It provides a gray scale 2D map, enhancing diffusion anisotropy differences with intensity limits between 0 and 1. A commonly used method to illustrate the direction of maximum diffusivity, however, is a color-coded FA-map in which the color of each voxel demonstrates its main diffusion direction [15]. Usually blue represents inferior-to-superior, red left-to-right, and green posterior-to-anterior diffusion direction (see *Figure 3*).

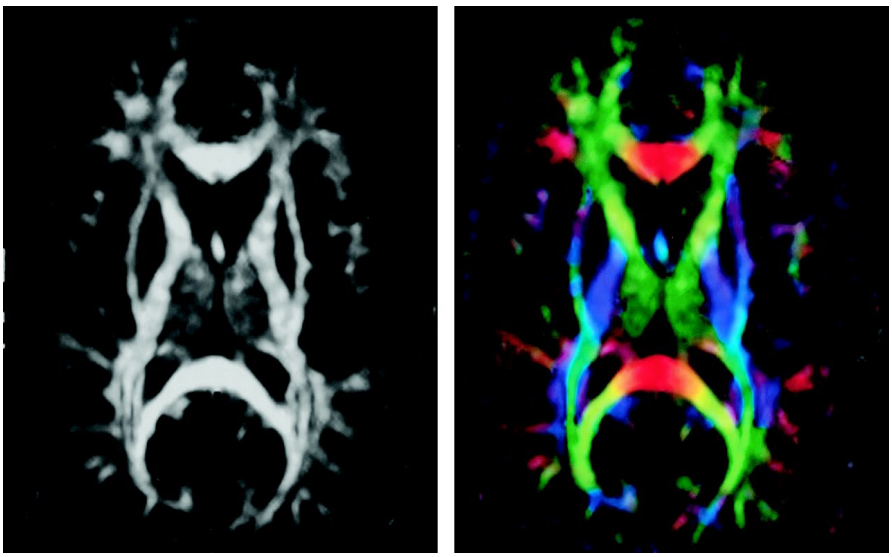

Figure 3 *- Fractional anisotropy maps without (left) and with directional information (right). Brightness is proportional to FA. The color-coding is described in the text* [13].

Another often used diffusion index in DTI simply is the *mean diffusivity* (MD) or *traceADC*. It can be calculated for each voxel by the mean of the three eigenvalues and corresponds to the molecular diffusion rate with lower values meaning lower diffusivity:

$$MD = \frac{\lambda_1+\lambda_2+\lambda_3}{3} = \frac{D_{xx}+D_{yy}+D_{zz}}{3} = \frac{Trace}{3},$$

where D_{xx}, D_{yy} and D_{zz} are the diagonal terms of the diffusion tensor [16]. Typically, the MD of damaged tissue is higher in comparison to normal tissue due to increased free diffusion. In contrast, FA usually decreases in damaged tissue because of reduced coherence in the main diffusion direction.

A third important application of DTI data to mention is *tractography*. With this method, a three-dimensional representation of white matter pathways or fiber bundles can be obtained from the principle eigenvector of diffusion for each voxel. The processing of tractography consists of *seeding*, i.e. defining the starting points from which the fiber bundles will be drawn, *propagation*, i.e. the fiber tracking process, and *termination* of the fiber tracking which is based on well-defined criteria [16].

Other, less often used DTI measures quantify myelin neuropathology (*radial diffusivity*) or axonal degeneration (*axial diffusivity*) [17].

2.2 Glioblastoma

GBM is the most common primary malignant tumor of the central nervous system (CNS). Histologically, it belongs to the greater group of *gliomas*, which comprise the majority of primary tumors within the brain parenchyma. The term glioma refers to the similarity of the tumors' cells to normal glial cells, i.e., astrocytes, oligodendrocytes, and ependymal cells. GBM represents the most aggressive subtype of glioma, referring to WHO (World Health Organization) grade IV, which has historically been labeled as "high-grade glioma".
Despite intensive treatment options GBM still carries a bleak prognosis. To date, there are no curative treatment options. Standard treatment follows the landmark *Stupp* trial of 2005 and initially consists of maximal safe surgical resection followed by radiotherapy with concurrent temozolomide chemotherapy, followed again by six cycles of maintenance temozolomide [18]. However, in the past decade there have been major advancements in the differentiated diagnosis of GBM (e.g., the 2016 WHO classification of CNS tumors) and in new patient-tailored treatment options. This chapter shall provide a systematic overview of the current state of clinical management and an insight into previous and recent milestones of research on GBM.

2.2.1 Epidemiology of glioblastoma

The annual incidence of gliomas is around 6 / 100,000 [19]. In Germany, there were approximately 6,700 cases of malignant brain tumors in 2014. Among adults, GBM accounted for more than two thirds of cases (see *Figure 4*). The median age of disease onset is 62 years for men and 66 years for women, respectively [20].
Many environmental and genetic factors have been studied but no risk factor has been identified which could account for a *relevant* proportion of GBMs. The majority are sporadic [21]. However, there are two known risk factors that increase the likelihood of developing brain cancer: One is ionizing radiation for another head or neck condition in the past. The other one is a positive family history. Studies showed that having an immediate relative with GBM doubled a person's risk of developing the same disease [22]. Moreover, people with certain inherited conditions, such as neurofibromatosis and tuberous sclerosis, are at an increased risk. However, such conditions cause only about 5% of gliomas [23].

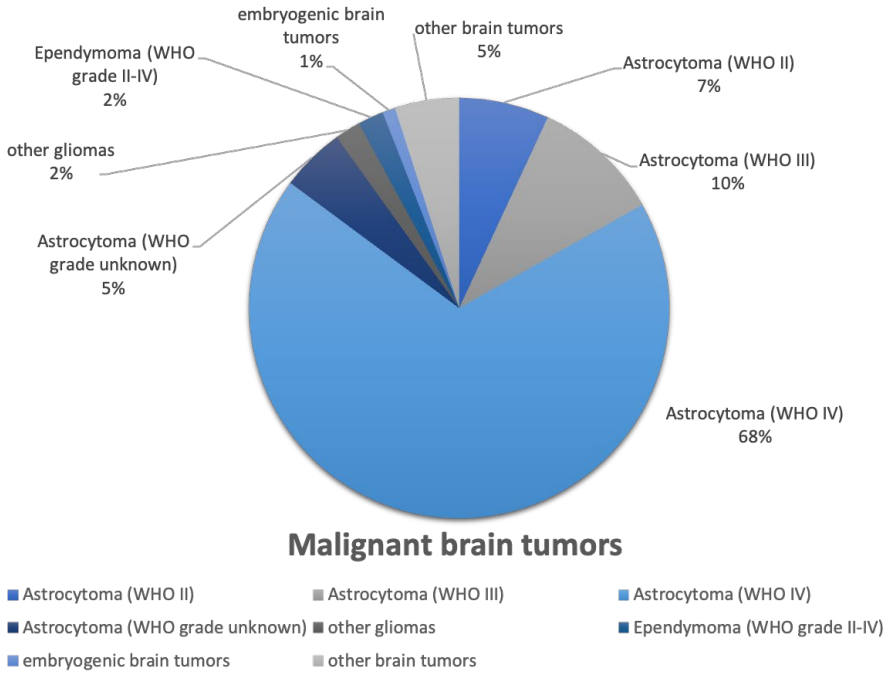

Figure 4 *– Distribution of the main histological subtypes of primary malignant brain tumors. Adults in Germany, 2012-2014. Data from* [20].

2.2.2 The 2016 WHO classification of tumors of the central nervous system

CNS tumors are divided into four different grades (I-IV) following the classification system of the WHO. These grades are defined by increasing degrees of dedifferentiation, anaplasia and aggressiveness. Historically, the slower-growing lesions (WHO grade I and II) have been referred to as *low-grade* gliomas, while the more rapidly progressive tumors (WHO grade III and IV) have been named *high-grade* gliomas. However, nowadays the WHO recommends avoiding these terms due to the heterogeneity of properties and prognoses within the groups. The classification was initially based on the histological characteristics of the tumors. The most recent version of the classification is the revised 4th edition released in 2016 [24]. This update is markedly different from its 2007 precursor. For the first time, it incorporates molecular characteristics into the classification. This approach is referred to as *integrated diagnosis*.

In terms of gliomas (see *Figure 5*), the most notable change is, that while in the past all astrocytic tumors had been grouped together, now all *diffusely infiltrating* gliomas belong to one group (whether their cells resemble astrocytic or oligodendroglial cells). This attribution is based on the tumors' growth pattern and behavior but also on the shared genetic driver mutations in the *IDH1* and *IDH2* (*isocitrate dehydrogenases 1* and *2*) genes. The presence or absence of *IDH1* and *IDH2* gene mutations now separates astrocytomas and glioblastomas into *IDH-mutant* and *IDH-wildtype* entitites. For the diagnosis of the common oligodendroglioma, on the other hand, in addition to IDH mutation, combined losses of the short arm of chromosome 1 and the long arm of chromosome 19 is necessary (*1p/19q codeletion*) [25].

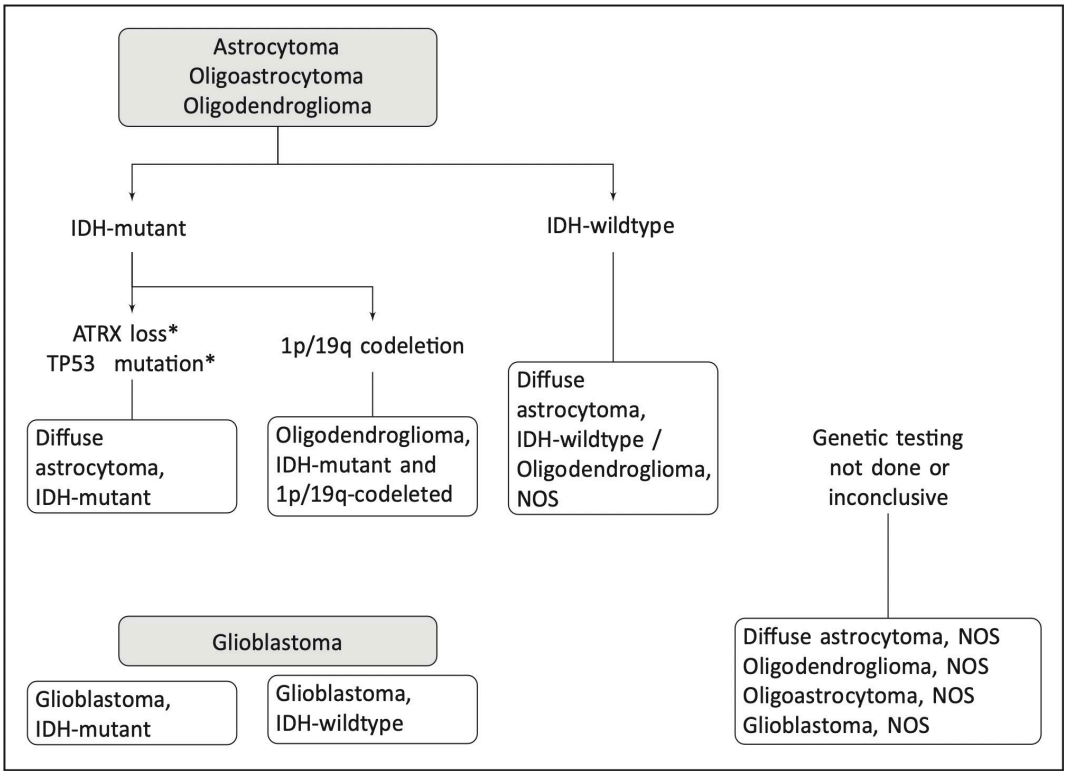

Figure 5 *- The 2016 WHO classification for tumors of the Central Nervous System. IDH mutation status and other genetic parameters classify the diffuse gliomas. The designation "not otherwise specified" (NOS) is used for tumors that either have not been fully tested for genetic alterations or have been tested but do not show the common diagnostic genetic alterations* [25].

The advantage of this dynamic classification is that it now groups tumors with similar prognostic markers and guides the use of therapies for biologically and genetically similar entities.

Glioblastomas, which are all graded as WHO grade IV tumors, are now divided into two subgroups: First, *glioblastoma, IDH-wildtype* (about 90% of cases), which mostly corresponds to the primary or *de novo* glioblastoma and is more common in patients of over 55 years of age. Second, *glioblastoma, IDH-mutant* (about 10% of cases) which often corresponds to secondary glioblastoma (deriving of a prior lower grade diffuse glioma) and preferentially affects younger

patients [26]. Between these two subgroups, MOS differs significantly from 15 months for *IDH-wildtype glioblastoma* to 31 months for *IDH-mutant glioblastoma* under maximal standard treatment consisting of surgery and radiochemotherapy. This demonstrates the prognostic value of this new, integrated diagnosis [26].

2.2.3 Standard treatment and recent developments

Patients diagnosed with GBM usually receive gross-total tumor resection. A 2016 meta-analysis of over 40,000 GBM patients showed that gross-total resection was associated with better survival in comparison to subtotal resection [56].

Microsurgical techniques are state of the art. There are several neurosurgical and imaging tools that help increasing the extent of resection and minimizing the risk of new neurological deficits. Those include navigation systems based on functional MRI datasets, intraoperative MRI, ultrasound, and intraoperative functional monitoring, as well as the fluorescent dye 5-aminolevulinic acid (ALA) to visualize tumor tissue [27]. When resection is performed in eloquent areas of the brain, evoked potentials, electromyography, or mapping in awake patients under local anesthesia can be used to monitor and preserve language and cognition. This is highly important since postoperative deficits due to complications are a negative prognostic factor [19].

Within 24-48 hours after surgery a post-operative CE-T1w (contrast-enhanced T1-weighted) MRI scan is routinely obtained to evaluate for tumor remnants since a study has shown that the radiological determination of the extent of tumor resection via MRI had massive prognostic significance [57]. Following surgery, since the implementation of the *Stupp* protocol, in most cases a combined radiotherapy with concomitant administration of temozolomide, a DNA alkylating agent, is added [18]. Initially, temozolomide (75 mg/m^2) is administered on days 1 through 42 with concomitant radiotherapy.

Radiotherapy plays a crucial rule in preserving function and increasing survival. Its indications, timing, dosing and scheduling is determined by diagnosis and prognostic factors, especially by the extent of resection [28]. The standard radiation dose of 50-60 Gy is usually administered in 30 fractions of 1.8-2.0 Gy. In elderly patients or those with poor prognosis, *hypofractionated* radiotherapy with higher fraction sizes and lower total dose, e.g., 15 x 2.67 Gy, is appropriate. Doses above 60 Gy have not shown to be beneficial, at least in the setting of whole-brain radiation [29].

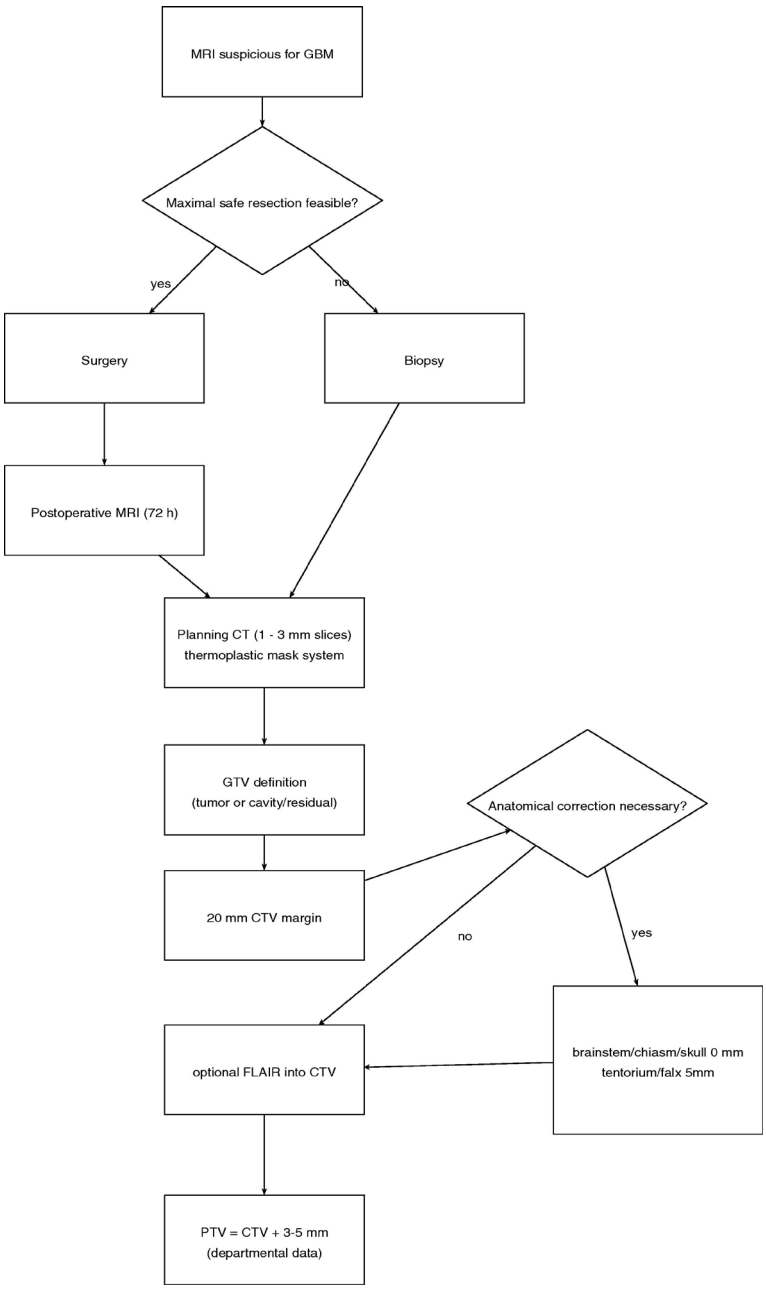

Figure 6*- Flowchart for delineating the planning target volume (PTV) according to ESTRO-ACROP guidelines of 2015. Abbreviations are explained in the text* [32].

For generating the planning target volume (PTV), no definite guideline has been established so far. Two major guidelines exist in parallel, one presented by the European Organization for Research and Treatment of Cancer (EORTC) and one that is recommended by the Radiotherapy and Oncology Group (RTOG). They mainly differ in the inclusion of surrounding Fluid Attenuated Inversion Recovery (FLAIR)-hyperintense edema and the addition of a radiation boost to the resection cavity and contrast enhancing tumor remnants in the 2-phase RTOG approach [30]. However, in trials that allowed application of both concepts, no significant difference in outcome is seen between these radiotherapy techniques [31]. Moreover, as a third possibility, radiotherapists often follow the current European joint consensus by ESTRO-ACROP (European Society for Radiotherapy and Oncology – Advisory Committee on Radiation Oncology Practice) (see *Figure 6).* It describes the clinical target volume (CTV) as gross tumor volume (GTV = residual enhancement on T1w imaging plus surgical bed) with a margin of up to 2.5 cm including the hyperintensity on T2w/FLAIR imaging which is modified to reduce radiation dose on critical structures and in areas where tumor spreading is unlikely. To that, another margin of 0.3-0.5 cm is added to account for error setup and patient

movement during radiation [32]. However, there are continuing controversies regarding the optimal volume delineation [33].

Modern techniques of focused radiotherapy, such as stereotactic, intensity-modulated or image-guided radiotherapy may improve patient outcome due to protection of surrounding tissue. To date, however, randomized data comparing such novel approaches with standard treatment are not yet available [19].

After a break of 4 weeks after initial radiochemotherapy, there usually follows another 6 cycles of 4 weeks temozolomide (150 – 200 mg/m^2 on days 1-5) each as maintenance therapy [18]. It is important to note that temozolomide only leads to a significantly prolonged survival in tumors exhibiting a methylated O^6–methylguanine-DNA methyltransferase (MGMT) - promotor since an unmethylated one makes the tumor cells resistant to the alkylating effect of temozolomide.

In case of tumor recurrence (which invariably occurs despite maximum treatment with the majority of recurrences being diagnosed within the first year [34]), standards of care are not yet defined. Repeated surgical intervention or reirradiation are highly individual decisions (considering general prognostic factors such as age and KPS), and significant data from randomized controlled studies are lacking. Most patients, however, receive temozolomide in standard dose, in combination with one of the available nitrosoureas carmustine (BCNU), lomustine (CCNU), or fotemustine, which are DNA alkylating agents as well. Again, the benefit of temozolomide in recurrent GBM seems limited to patients with MGMT promotor methylation [35].

In 2009, the anti-vascular endothelial growth factor (VEGF) A-antibody bevacizumab has been approved by the FDA (Food and Drug Administration) in the United States for the treatment of recurrent GBM on the basis of uncontrolled data. Higher median PFS and higher MOS were reached in 2 of 3 retrospective studies favoring reirradiation combined with bevacizumab in comparison to reirradiation alone [36]. The recent EORTC 26101 phase III trial did not report a difference in MOS comparing lomustine plus bevacizumab with lomustine alone in patients with recurrent GBM, although prolonged PFS was confirmed [37]. Therefore, its utilization remains controversial and further molecular and neuroimaging research should aim to identify patients who might benefit from that treatment.

Immunotherapeutic treatment options are currently under evaluation for both newly diagnosed and recurrent GBM with partially promising preliminary data which warrant further efforts [36].

2.2.5 Prognosis

The 5-year survival rate for GBM patients averages 5.8% [1]. Most disease-associated deaths occur in the 5th quarter postdiagnosis. However, patients surviving past 2 years from diagnosis have a relatively favorable conditional probability of survival into the future [38]. Since the implementation of the *Stupp* protocol (co-administration of temozolomide and radiation) there has been a remarkable increase in survival (from 13.5 months to 15.6 months MOS) [1]. The median survival without any treatment is only 3 months, indicating the high malignancy of this tumor entity [39].

Essentially all patients develop recurrence or progressive disease after initial treatment. The median PFS is between 6 and 9 months, depending on therapy and molecular status [2]. The MOS at recurrence is approximately 6 months [40].

2.3 Standard and Advanced Imaging of Glioblastoma

The last part of the theoretical section shall give the reader a concise overview of the standard imaging protocol for suspected brain tumors. Furthermore, it covers some advanced imaging techniques that are increasingly utilized in the clinical setting because of the benefit they bring to diagnostic precision. It is divided into two parts. A first part focuses on the preoperative setting, whereas the second part illuminates the challenges of postoperative imaging when treatment response has to be evaluated and progress needs to be distinguished from treatment-associated changes.

2.3.1 Preoperative evaluation of the brain tumor

Most patients with GBM receive a CT scan of the brain when they initially present at the hospital (see *Figure 7*).

When a mass is identified and hemorrhage of the brain is ruled out, a contrast-enhanced MRI examination of the patient is usually performed. The minimum standard protocol [41] consists of T2-weighted (**T2w**), T2-fluid attenuated inversion recovery (**T2w-FLAIR**), **DWI**, T1-weighted (**T1w**), and T1-weighted contrast-enhanced (**CE-T1w**) sequences. In addition, most institutions perform high-resolution MRI (0.5-1.2 mm slice thickness) that is utilized by neurosurgeons for surgical planning and intraoperative guidance [42]. DWI is usually incorporated in standard imaging protocols because it alleviates the differential diagnosis of cystic brain lesions: Brain abscesses, epidermoid tumors and lymphomas typically show high signal intensity on DWI and low ADC values, while cystic / necrotic tumors and metastases, arachnoid cysts and toxoplasmosis usually show similar signal intensity to CSF on DWI. This is due to the differences in cell density and cellularity between these entities. The higher the cellularity or cell density (e.g., with very high values in lymphomas), the more diffusion is restricted. However, necrotic tumor and cystic metastases may occasionally show restricted diffusion as well, it has especially been documented for metastatic squamous cell carcinoma and radiation necrosis. In unclear cases, Magnetic Resonance Spectroscopy (MRS) may be useful for a definitive diagnosis [43].

Standard imaging provides a lot of relevant biological information about the tumor mass. Those include the volume of the different tumor sub-regions (i.e., necrotic, enhancing, and non-enhancing tumor), compression of the surrounding peritumoral tissue and the risk of toxicity to nearby *eloquent* regions (i.e., cortex areas which directly control function and will lead to major focal neurological deficits if damaged), and midline deviation due to mass effect. Moreover, on T2w-FLAIR images the extent of the peritumoral edema can be assessed. This white matter edema develops in response to angiogenic and vascular permeability factors which are associated with infiltrating tumor [44]. Its potential in estimating tumor invasiveness and recurrence probability will be discussed later (see *Section 5*).

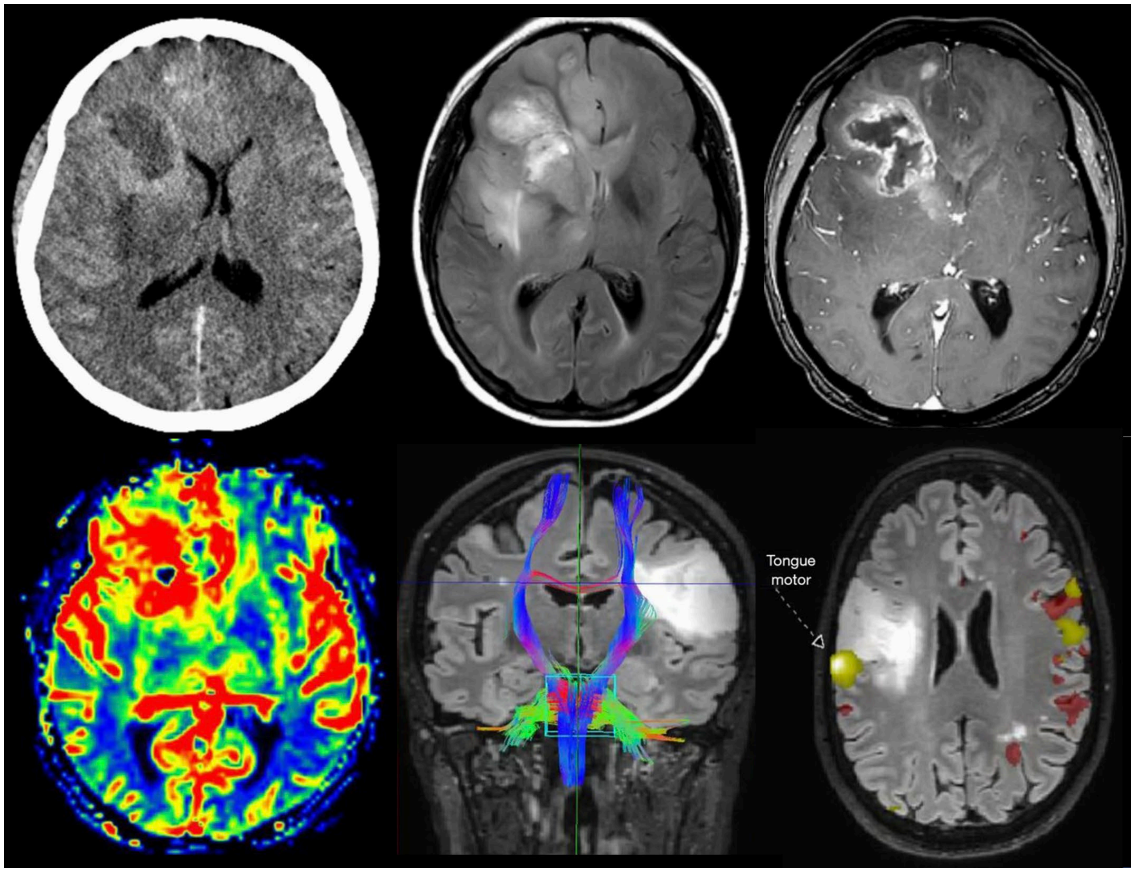

***Figure 7** – Extracts from sets of imaging studies acquired for different glioblastoma patients. Top row: Standard images showing a right frontal intracranial mass with contrast enhancement in axial slices (from left to right: CT, T2wFLAIR, CE-T1w) Bottom row: Three examples of advanced imaging modalities (from left to right: PWI (Cerebral Blood Volume), DTI tractography, fMRI)* [42].

Some advanced imaging methods are increasingly used in the preoperative setting as well. Functional MR imaging (**fMRI**) might be utilized for surgical planning in cases where tumors or their resection might disrupt eloquent areas (see *Figure 7*) [45].

Another common method to guide surgical planning is to use **DTI** which generates white matter tractography images that can be used for intraoperative navigation as well (see *Figure 7*) [46]. DTI also helps to differentiate intra-/ post-operative vascular damage from residual enhancing

tumor [47] and it has been subject to numerous studies examining its ability to distinguish different brain gliomas, metastases, and lymphomas, from each other and different, non-malignant pathologies of the brain [48]. In our study, DTI has been used to predict the localization of later tumor recurrence in the preoperative MRI by assessing the peritumoral edema for early alterations. This will later be discussed in detail.

Furthermore, perfusion weighted images (**PWI**) parameters can be used in the preoperative setting to evaluate tumor characteristics (see *Figure 7*). In general, PWI techniques assess hemodynamic parameters derived from a time-intensity curve following contrast agent injection. Therefore, they can detect pathological alterations of tissue vascularity, such as in brain tumors, which in these cases are mostly due to increased vascular permeability or tumor-induced angiogenesis. Dynamic contrast enhancement (**DCE**) and dynamic susceptibility contrast (**DSC**) sequences have both been utilized in studies to assess for early disease progression and survival [49], and tumor type prediction or glioma grading, respectively [50].

As mentioned above, **MRS** is another useful tool for the diagnosis of malignant brain tumors (see *Figure 8*). Basically, it noninvasively measures concentrations of metabolites within tissues. In the context of preoperative imaging of brain tumors, it especially helps to exclude differential diagnoses with markedly different spectroscopic patterns which may look similar on conventional MRI, such as strokes, brain abscesses, or focal cortical dysplasias. MRS has also been suggested as a tool to discriminate solitary metastases from primary brain tumors by assessing the peri-enhancing tumor regions: While gliomas often show elevated Choline levels in the surrounding brain tissue, metastases tend to be more encapsulated and do not usually show high Choline signals outside the region of enhancement [51]. Generally, the combination of post-contrast MRI, DWI, PWI, and MRS has been shown to improve the diagnosis and classification of intracranial masses [52].

18F-fluorodeoxyglucose (18F-FDG) positron emission tomography (**PET**) plays a crucial role in oncologic imaging. However, due to the high background uptake by the normal brain its diagnostic relevance in brain tumor imaging has been quite limited. However, more recently, specific amino acid PET tracers, such as ^{11}C-methionine, 18F-fluorothymidine (FLT), 18F-fluoro-ethyl-tyrosine (FET), 18F-dihydroxyphenylalanine (DOPA) have been introduced. Their high lesion-to-background uptake ratios make them suitable for different applications in brain tumor imaging, such as predicting tumor grade, detecting recurrent tumor, and assessing treatment response [53].

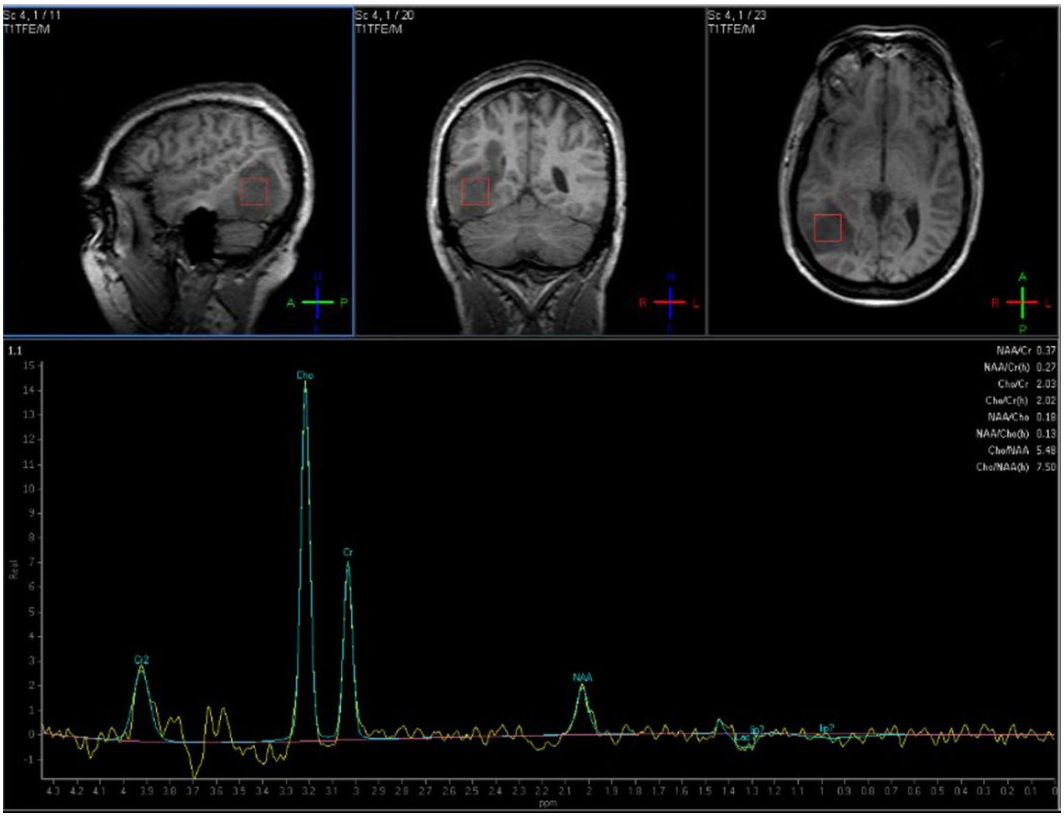

Figure 8 *- Single voxel MR spectroscopy at long TE (228 ms). MRI appearance is compatible with a glial neoplasm in the right temporoparietal region. There is markedly elevated choline (resonates at 3.2 ppm) and markedly decreased NAA (N-acetyaspartate, resonates at 2 ppm). These findings are consistent with high grade glioma* [42].

Another advancement of brain tumor imaging is due to the increasing computing power and availability of pre-engineered algorithms which made it possible to analyze signal intensity variations on a voxel-to-voxel level. With this information, imaging features can be correlated with tumor biology / phenotypes and treatment response. This type of biomarkers, called *radiomics*, carries potential in evaluating especially high-grade gliomas with their genetic heterogeneity and complex imaging phenotypes [54]. For example, the integration of multiple conventional MR image parameters using *machine learning* (ML) based approaches has shown promising results in predicting WHO grade of gliomas [55]. Furthermore, IDH mutation status has shown to be predictable by using MRS driven measurement of 2-hydroxyglutarate (2HG) [56], static and dynamic FET-PET measurements [57], and also by applying ML algorithms on conventional MRI data [58][59].

2.3.2 Response assessment in postoperative imaging

Following standard treatment as explained above, 20-30% of patients with GBM develop increased contrast-enhancement within 3 months after the end of radiotherapy which subsides

without any change of treatment [60]. This effect is termed *pseudoprogression*. It likely results from transiently increased permeability of the tumor vessels due to irradiation and may be enhanced by temozolomide administration. It is important to not mistake this for true tumor progression since treatment with potentially beneficial adjuvant temozolomide might be erroneously stopped and patients might be included in trials of progressive or recurrent glioma inappropriately. To mitigate this problem the Response Assessment in Neuro-Oncology (RANO) criteria have been developed in 2010 [60]. They require a minimum of 12 weeks after completion of radiochemotherapy before progressive disease can be confirmed unless the location of increased contrast enhancement is distant from the radiation field or there is pathologic evidence of progressive or recurrent tumor. In the last decade, tremendous efforts have been put into improving the diagnosis of *pseudoprogression*. For example, it has been shown that recurrent or progressive tumor more commonly shows lower ADC values in comparison to normal brain tissue or necrosis [61]. Moreover, recent studies demonstrated that a voxel-vise analysis of ADC maps can differentiate *pseudoprogression* from true progression by utilizing a newly introduced postprocessing tool called *ADC parametric response maps* [62]. Other approaches found that *pseudoprogression*, compared to true tumor progression, exhibits lower relative blood volume in DSC-MRI [63] and significantly lower 18F-FET uptake [64]. And also MRS using choline to N-acetylaspartate (NAA) ratio has been shown to distinguish glioma progression from radiation necrosis with a sensitivity and specificity of 0.88 and 0.86, respectively [65].

Another post-therapeutic phenomenon to consider is *pseudoresponse* after antiangiogenic therapy. The monoclonal antibody against VEGF, bevacizumab, and similar agents can result in rapid normalization of vascular permeability which may reduce the intensity of contrast enhancement on T1w MRI. However, this phenomenon is not associated with improved patient survival [66]. A subset of patients treated with bevacizumab have been shown to develop tumor recurrence characterized by an increase in the non-enhancing component. Therefore, the RANO criteria also require evaluation of the non-enhancing T2/FLAIR-hyperintense tumor. There are multiple promising approaches to enhance investigation of tumor progression under antiangiogenic therapy, e.g. T1 subtraction mapping [67] or ADC threshold values to differentiate hypercellular progressive tumor and necrosis [68].

Addressing the emerging use of immunotherapeutic treatment options, the RANO group has already published a guideline for the assessment of radiological changes following immunotherapy, called the *iRANO criteria* [69].

3 Materials and Methods

3.1 Patient Acquisition and Imaging Protocol

For the study, 35 glioblastoma cases from this institute's prospective glioma cohort were selected. This was approved by the local ethics committee. Criteria for inclusion were availability of pre- and postoperative DTI data (2 mm isotropic resolution, TE = 78 ms, TR = 5000 ms) with 32 directions (b = 800 s/mm^2) and one non-diffusion-weighted $b0$ volume (N_b= 32) besides the standard MRI protocol for brain tumor diagnosis: T2 turbo spin echo (T2w), T2-FLAIR, non-enhanced and contrast-enhanced T1 (T1w and CE-T1w). Availability of MR images showing (first) tumor recurrence was also mandatory. All cases underwent histopathological examination and were diagnosed as IDH-wildtype glioblastoma according to the 2016 WHO classification of brain tumors [24]. All patients were scanned in a 3 T whole-body MRI scanner (Achieva or Ingenia, Philips Medical Systems, Best, The Netherlands).

3.2 Semi-automatic tumor segmentation and image registration

The preoperative as well as the first postoperative MR scan showing tumor recurrence were semi-automatically segmented into FLAIR-hyperintense and contrast-enhancing areas of the tumor by using an in-house-developed segmentation algorithm (see *Figure 9*).
This algorithm comprises a generative probabilistic model for brain tumor segmentation which is based on Bayesian clustering. It then uses Gaussian copulas to capture dependencies between the intensities in the different input modalities. Finally, two random forests are included to generate robust label prior maps for the model, and to ensure spatial coherence in the segmentations, respectively. It also includes two semi-automated extensions to allow the user to interactively guide the segmentation [70].
Where necessary, segmentation masks were manually corrected using ITK-SNAP, a general-purpose interactive tool for image visualization, manual segmentation and semi-automatic segmentation [71]. To align the preoperative scans with the postoperative exam showing tumor recurrence, nonlinear co-registration (SyN, [72]) was applied using the open-source toolkit ANTs (advanced normalization tools for brain and image analysis) (https://github.com/ANTsX/ANTs). While linear registration only globally translates, rotates, zooms and / or shears one image to match it with another, nonlinear registration accounts for

deformable and voxel-wise image transformation and local misalignment which is especially useful in images with local abnormalities like tumors. SyN (symmetric image normalization) is a nonlinear symmetric diffeomorphic registration technique that matches images well by first performing an affine registration algorithm, which is a subtype of linear registration, for initialization, and then applying a nonlinear SyN registration algorithm.

In a next step, the segmentation of tumor recurrence was warped onto the preoperative MR image using nearest-neighbor interpolation, also utilizing the ANTs framework. In this technique, missing voxel intensities in the output image are estimated based on their immediate neighbors, guaranteeing a transformed image which matches the intensity distribution of the original moving image.

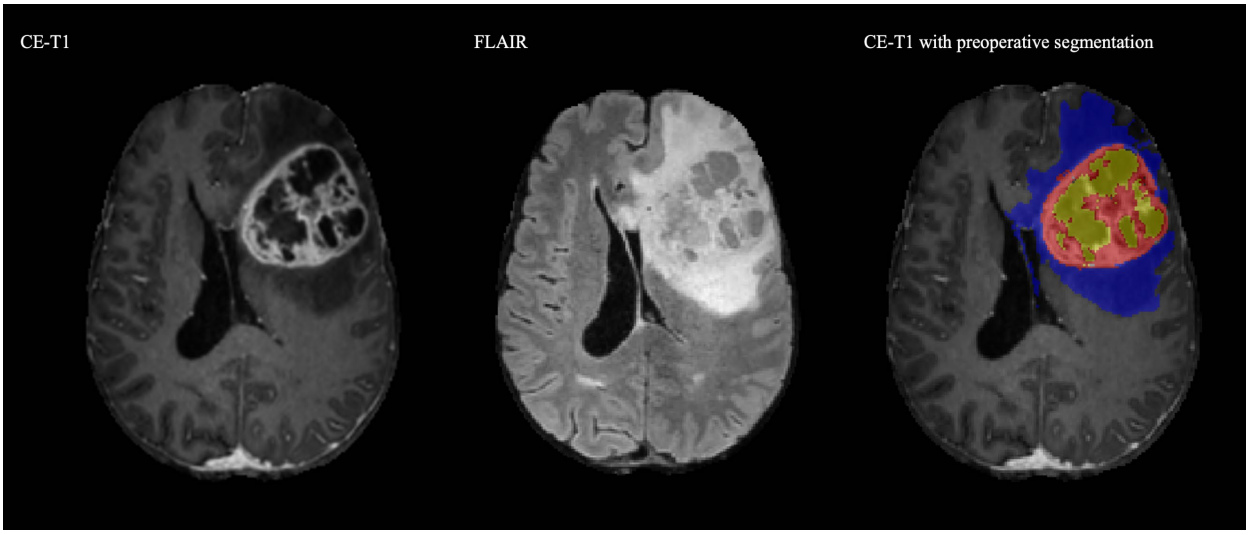

Figure 9 *- Preoperative semi-automatic segmentation in one glioblastoma case. The image on the left shows the raw CE-T1w image, the picture in the middle depicts the FLAIR image of the same slice. On the right, there is the segmentation mask overlaid on the CE-T1w image. Peritumoral edema is marked in blue, the contrast-enhancing areas are red-labeled and yellow denotes necrotic tumor core.*

Thus, both segmentation masks (the one of the primary tumor and the one of the tumor recurrence) were combined in the preoperative image space, which allowed for objective extraction of DTI parameters from every voxel of the image space. The benefit of this method was that there was no need for manual region-of-interest (ROI)-placement which has the disadvantage of being subjective and unreliable.

3.4 Free-Water Correction of DTI Data

The methodology of FWC has first been described in 2009 by Ofer Pasternak et al. [5]. In this context, *free-water* is defined as water molecules in the brain that are not restricted by their surroundings and do not flow. It is found as CSF or vasogenic edema in the extracellular space due to leakiness of the blood-brain barrier caused by tumors, brain trauma or hemorrhage [73]. Free-water can be identified using DTI by showing isotropic values of the ADC of about $3 \cdot 10^{-3}$ mm^2/s for 37°C which is almost 4 times larger than the typical ADC values of the brain parenchyma [74]. However, if a voxel contains more than one tissue type, e.g., free-water and white matter, DTI indices only reflect the weighted average of all compartments (*partial volume effect).* This hinders the evaluation of areas with such partial volume effects, for example the delineation of fiber tracts along the ventricles as well as the identification of the underlying tissue condition in areas with vasogenic edema. Commonly, FLAIR-DWI has been used to eliminate CSF contamination but it shows several drawbacks, including: It reduces the *signal-to-noise ratio* (SNR), increases scan time and it usually does not correct edema contamination due to different relaxation times [75]. Since in our project, the underlying tissue of voxels contaminated by vasogenic edema is the point of interest (as most recurrences occur closely to the initial tumor site in the peritumoral edema) we decided to apply FWC, which instead uses a bi-tensor model to get tissue-specific diffusion indices for each voxel and to obtain a voxel-wise map of the amount of free-water. FWC uses a two-compartment tissue model composed by tissue and free-water. For each voxel, the diffusion signal is modeled along the diffusion directions as the contribution of tissue and free-water components, thus disentangling the "true" diffusion signal from the contamination by free-water.

Fitting the diffusion tensor in a two-compartments model is an ill-posed problem. This has been solved using spatial regularization or optimized acquisition protocols before [76]. However, these approaches are limited by the availability of rich datasets. Therefore, here we used a new method based on an ANN that is trained with synthetically generated data and can be applied retrospectively to any diffusion MRI data. The method is briefly summarized below, following previously published work of our working group [7].

3.4.1 Synthetic signal modelling

In a first step, a mathematical framework is established to generate unlimited synthetic diffusion signals, containing known amounts of free-water partial volume effects, as training set for the

ANN. The random variables in this model are the diffusion signals of the tissue component S_t and the volume fraction of free-water f_{fw}. The other variables of the model are known, depending on the diffusion metrics and the random values of S_t and f_{fw}. They follow a simplified equation defining the diffusion signal of a single voxel S:

$$S(b, \boldsymbol{g}) = S_0 \left(f_t S_t(b, \boldsymbol{g}) + f_{fw} S_{fw}(b, \boldsymbol{g}) \right),$$

where b and $\boldsymbol{g}$ summarize the gradient effects of the diffusion weighted image, S_0 is a scaling factor proportional to the proton density, and f_t and f_{fw} are the volume fractions of tissue and free-water, respectively. S_{fw} is considered known due to the well characterized diffusion properties of free-water at body temperature showing isotropic diffusion with a diffusion coefficient of D_{fw}= 3 x 10^{-3} mm^2/s and $S_{fw}(b,\boldsymbol{g})$ = e^{-bD_fw}.
S_t and f_{fw} are represented as random variables of a uniform distribution U (0,1).

3.4.2 ANN architecture

The purpose of the ANN is to estimate the tissue volume fraction f_t directly from the raw diffusion signal $S(b,\boldsymbol{g})$. It is designed as a regression fully connected ANN with an input layer

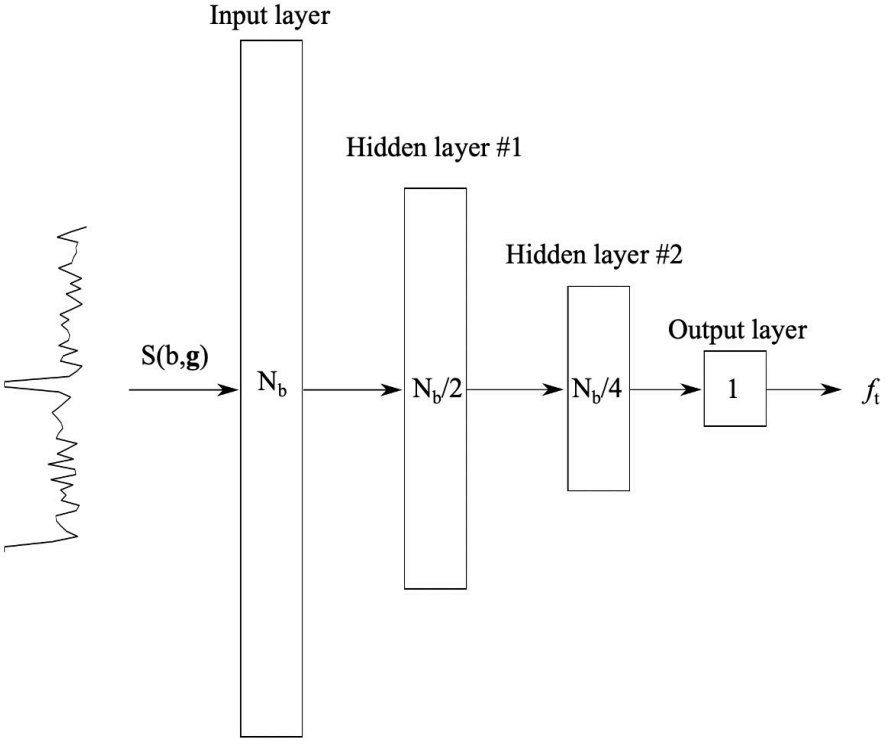

Figure 10 *- Illustration of the artificial neural network. The single components are explained in the text.*

of as many units as the number of acquired *b*-values (including non-diffusion-weighted volumes), N_b, and a single output unit yielding the estimate of f_t. The ANN is composed in a pyramidal structure with two hidden layers with $N_b/2$ and $N_b/4$, respectively (see *Figure 10*).
To train the model, 2000 synthetic signals (as described above) were used, with 70% for training, 15% for validation and 15% for testing. Convergence was reached after nine epochs and 4.7s in a consumers' laptop (Apple MacBook Pro, Intel Core i5, 8GB RAM; MATLAB, Mathworks, Natwick, MA). In comparison with the state of the art methods of Pasternak et al. [5] and Hoy et al. [76], the ANN results were equivalent or even less over-regularized in the case of MD estimations [7]. Afterwards, *robust estimation of tensors by outlier rejection* (RESTORE) was employed for tensor estimation to extract DTI metrics both from the FWE data and the standard DTI data [77]. This method uses iteratively reweighted least squares regression to exclude potential outliers prior to tensor estimation. The major advantage of this approach is that it takes into account the signal variability of not only thermal noise (= *Brownian motion*), but also artifacts from "physiologic noise" due to subject motion, cardiac pulsation and acquisition-related factors.

3.5 Data Collection and Statistical Analysis

The purpose of this work was to find a new way to predict the exact localization of tumor recurrence. Therefore, the peritumoral edema was the region of interest that was assessed for alterations in MD and FA values before and after FWC in a way that was also described in a previously published paper of our working group [78]. In particular, following the analysis by Bette et al. [79], eight 3 x 3 x 3 mm patches from the peritumoral edema of each patient were randomly sampled, of which four showed later recurrence and four did not. Afterwards, the 10^{th}, 50^{th}, and 90^{th} percentile, as well as the mean of MD and FA values were automatically extracted from these patches, both for original and FWC DTI data. In a next step, three generalized mixed-effect models (with *patient* being the random effect) were fitted to predict later recurrence: One, using only FWC FA values from the patches, a second, using only noncorrected FA values, and a third, using both values. To minimize the bias while fitting the models, threefold cross-correlation was applied. Furthermore, DeLong's test was used to compare correlated receiver-operating-characteristic (ROC) curves. All statistical analyses were done in Python (3.6) and R (3.6).

4 Results

Some of the results in this chapter have been published in the Special Issue "Tumors of the Central Nervous System: An Update" of the MDPI-journal *Cancers* in March 2020 [78].

4.1 Tissue Volume Fraction Estimates

The ANN was trained to estimate the fractions of free-water and tissue, respectively, in each voxel from the measured diffusion signal. Therefore, in a first step, we generated tissue volume maps (TVM) that visualized the amount of tissue in each voxel (see *Figure 11).* As one would expect, the tissue volume fraction approximates zero in CSF of the ventricles and is very high in healthy gray and white matter. In the area of the brain tumor, however, the fraction of tissue is the lowest inside the necrotic core of the tumor. Concerning the non-enhancing part of the tumor, the TVM show an inhomogeneous pattern.

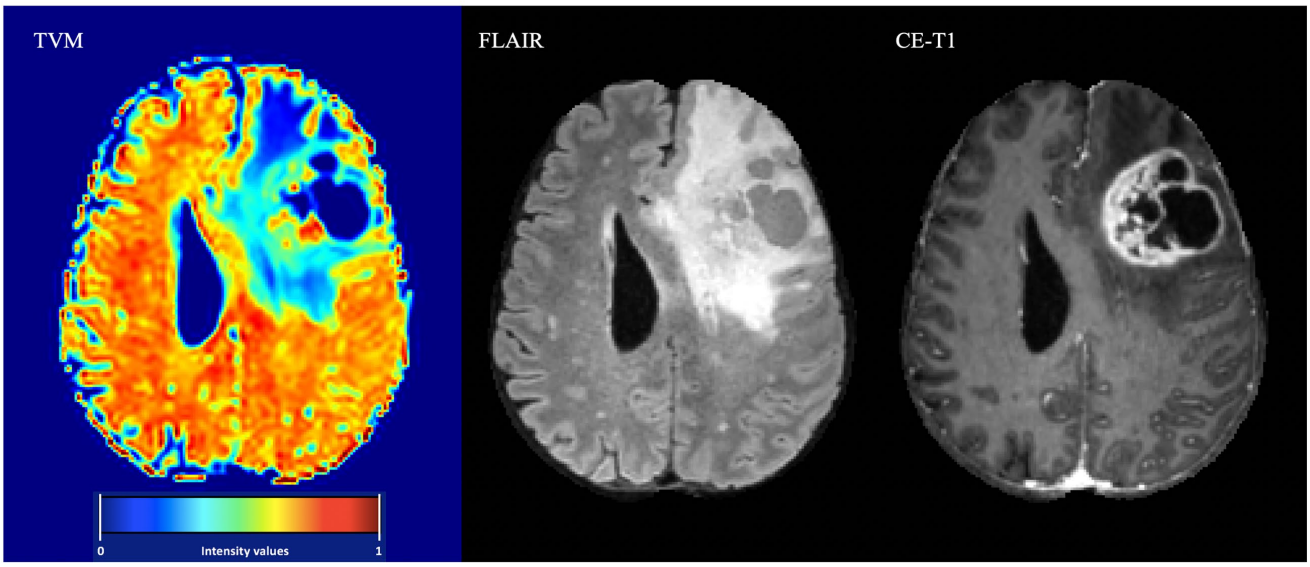

Figure 11 *– One example of a TVM in a patient with left frontal GBM. Observations are described in the text. A FLAIR and a CE-T1w image of the same slice is added for reference.*

Therefore, we were interested in whether or not there might be alterations in the amount of tissue in voxels of those parts of the peritumoral edema on preoperative MR images that showed later tumor recurrence (see *Figure 12*). Thus, we performed statistical analysis of the tissue volume fractions obtained from the recurrence- and the non-recurrence-part of the peritumoral

edema. However, there were no significant differences in the 10th, 50th, or 90th percentile of tissue volume fraction values (see *Table 1* and *Figure 13*).

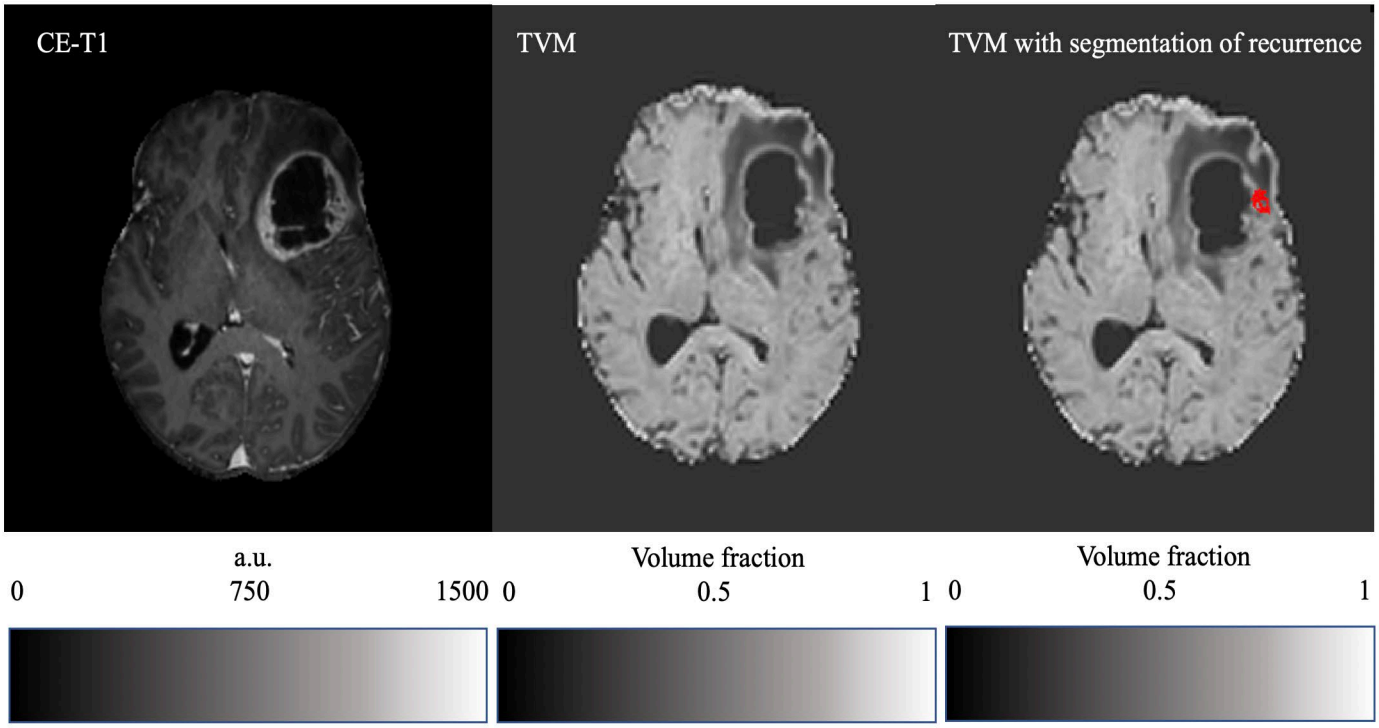

Figure 12 *- Tissue volume maps. For reference, a preoperative CE-T1w image is depicted on the left. The image in the middle shows the preoperative TVM. In the image on the right, the segmentation mask of the postoperative recurrence is added in red.*

Percentile of Tissue Volume Fraction values	*CET*	*Recurrence*	*Edema*	*p-value Edema vs. Recurrence*
10th	0.32948	0.29437	0.28969	**0.41430**
50th	0.51801	0.51203	0.47913	**0.42105**
90th	0.71627	0.73903	0.77102	**0.39444**

Table 1 *- Comparison of different percentiles of tissue volume fraction values between contrast-enhancing tumor (CET), edema with later tumor recurrence and pure peritumoral edema.*

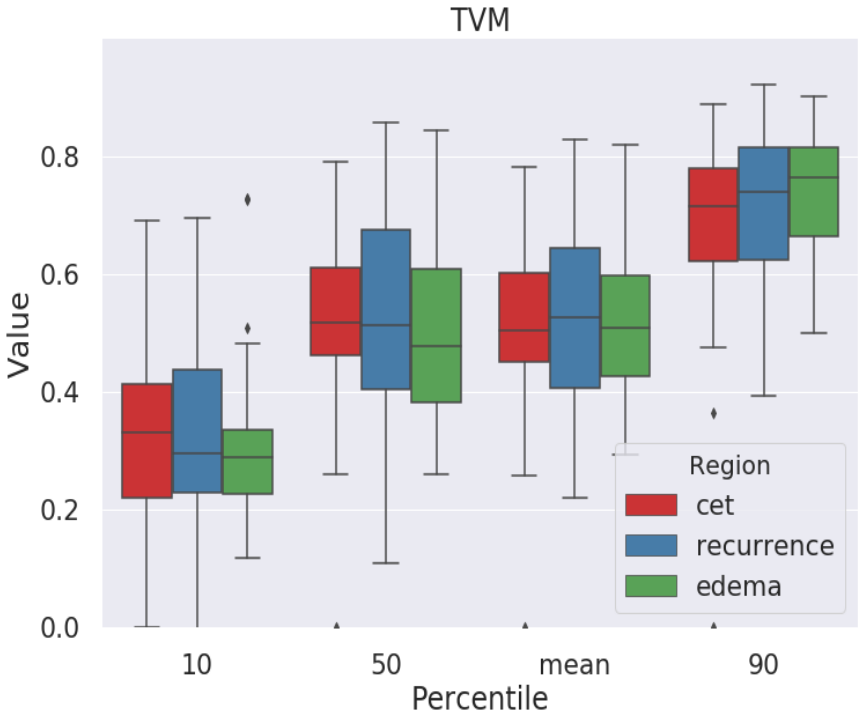

Figure 13 *– Tissue volume fractions of contrast-enhancing tumor (red), area of peritumoral edema with later recurrence (blue) and pure peritumoral edema (green). Diamonds denote outliers.*

4.2 Free-Water Corrected Mean Diffusivity

Subsequently, we examined MD values after performing FWC as described above and compared them with the original MD values in analyzing peritumoral edema. The hypothesis was that there might be significant differences in FWC MD values between areas with later tumor recurrence on postoperative MR images and areas with "pure", later recurrence-free edema.

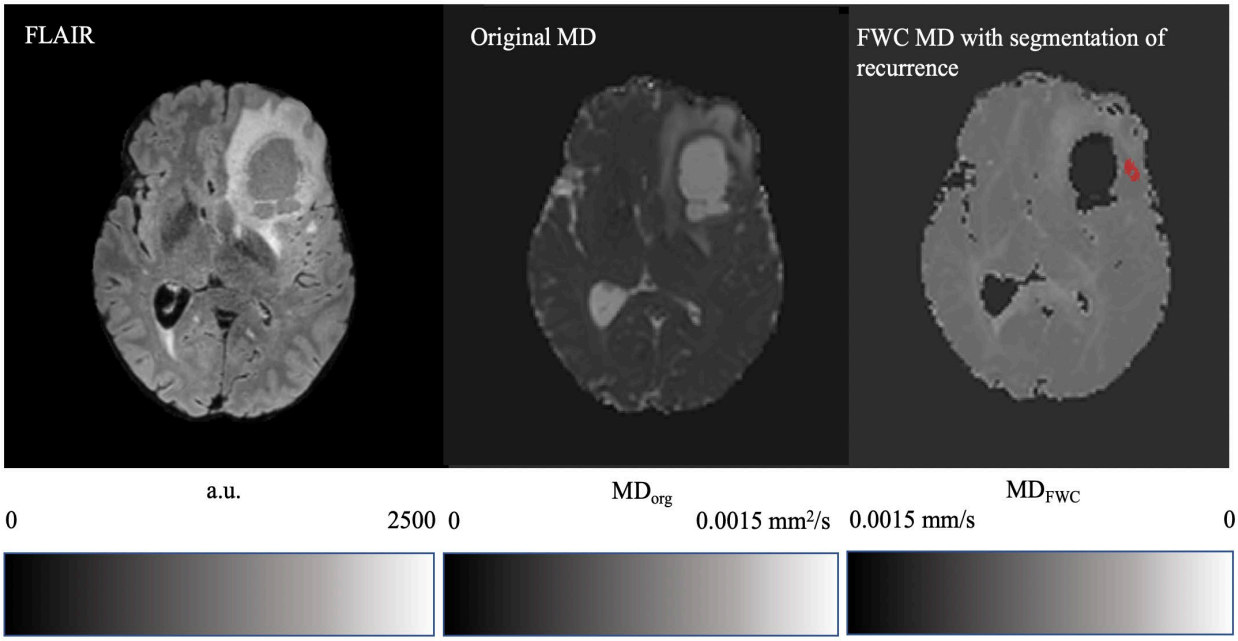

Figure 14 *- Mean Diffusivity maps of a preoperative MRI examination. For reference, a FLAIR image showing the tumor region is depicted on the left. Since FWC clearly decreases contrast, in the FWC MD map showed on the right, contrast is inverted to ease evaluation.*

However, these differences appeared to be rather small and were only significant in the 90th percentile of FWC MD values with lower values in the areas of later recurrence (p_{90} = 0.04649). In contrast, without applying FWC there were no significant differences between both types of edema at all (p_{90} = 0.16753). The results are summarized in *Table 2* and *Figure 15*. It is noticeable that FWC clearly decreased the contrast of MD maps (see *Figure 14*). This effect will be discussed later (see *Section 5.2*).

Percentile of Mean Diffusivity values	*CET*	*Recurrence*	*Edema*	*p-value Edema vs. Recurrence*
Free-Water Corrected DTI data				
10th	0.00060	0.00060	0.00061	0.80062
50th	0.00064	0.00063	0.00065	0.15018
Mean				0.23317
90th	0.00068	0.00067	0.00070	**0.04649**
Original DTI data				
10th	0.00091	0.00090	0.00086	0.30961
50th	0.00121	0.00119	0.00139	0.19837
Mean				0.24728
90th	0.00159	0.00164	0.00177	0.16753

Table 2 *- Comparison of Mean Diffusivity values between contrast-enhancing tumor (CET), edema with later tumor recurrence and pure vasogenic edema with and without free-water correction.*

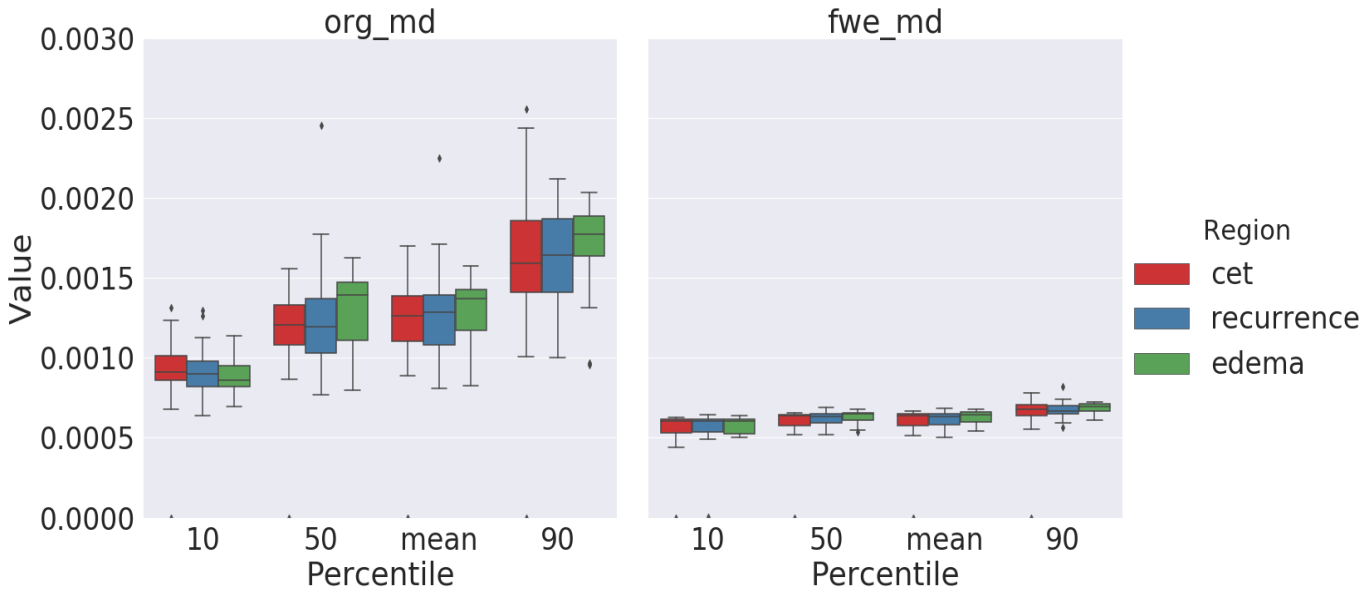

Figure 15 *- Original Mean Diffusivity values (left) and Mean Diffusivity following free-water elimination (right) of contrast-enhancing tumor (red) and peritumoral edema with (blue) and without (green) later tumor recurrence. Diamonds denote outliers.*

4.3 Fractional Anisotropy Recovery

Visually comparing FWC FA maps with the original ones, there is a relevant improvement of FA information, especially in areas with large partial volume contamination of free-water. Especially at the borders of the ventricles and in the area of peritumoral edema one can suspect more information about the underlying tissue from the more pronounced shading of the FWC FA maps (see *Figure 16*).

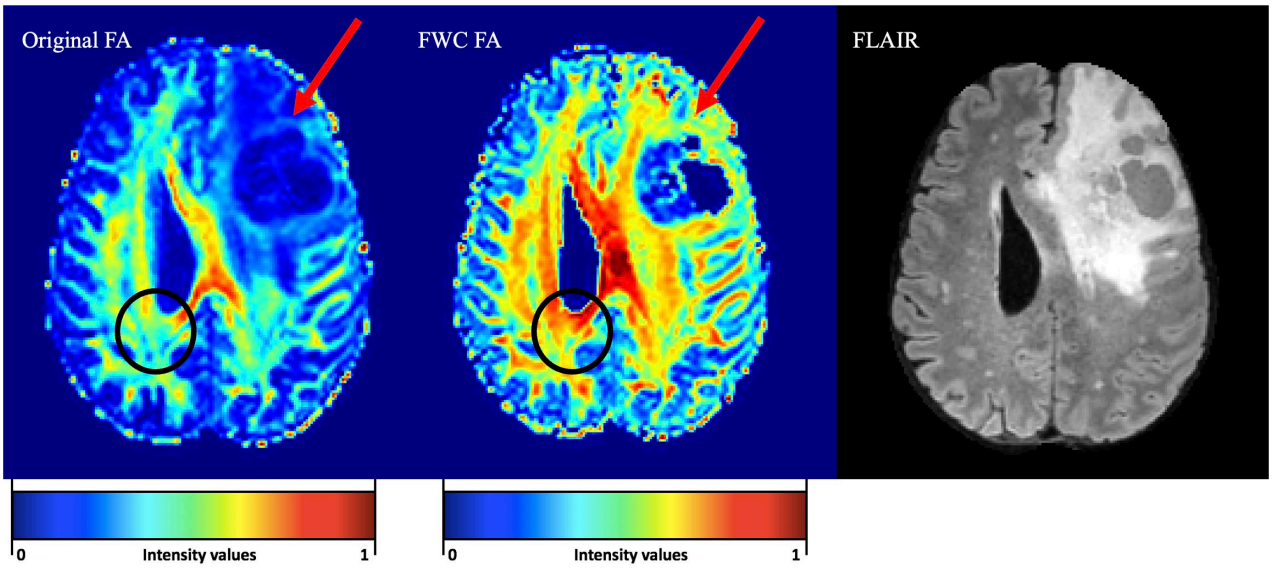

Figure 16 *– Visual improvement of FA maps due to FWC. Especially in areas with partial volume effect of water, for example at the boarders of the ventricles (black circles), or in the peritumoral edema (red arrows), more information is recovered. The preoperative FLAIR image on the right illustrates the extent of the peritumoral edema of the left frontal GBM.*

Therefore, we evaluated this new information for its applicability in predicting the localization of tumor recurrence. Again, we compared FA values of areas within the peritumoral edema which showed later tumor recurrence and recurrence-free edema (see *Figure 17*).

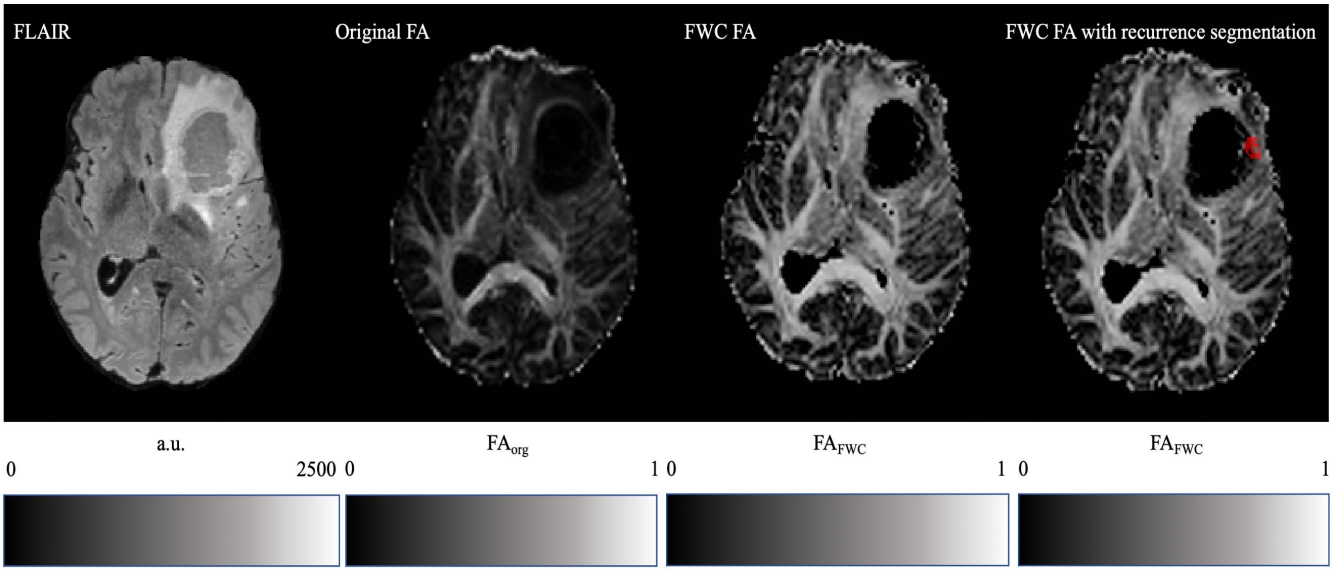

Figure 17 *-Comparison of original and FWC FA maps in gray scale. For reference, again the preoperative FLAIR image is added on the left. FWC of FA maps reveals more information about the tissue microstructure in the area of peritumoral edema. As a special region of interest, the recurrence site is marked in red in the image on the rightmost.*

The 10th, 50th, and 90th percentile of the FWC FA values, as well as their mean values showed significant differences between both types of edema with $p_{10} = 0.00112$, $p_{50} = 0.00314$, and $p_{90} = 0.00007$. In particular, FA values of regions with later tumor recurrence were significantly lower than those of recurrence-free edema, indicating some disturbance of the tissue-microstructure integrity.

In contrast, the original, noncorrected FA values only showed significant differences in the 90th percentile ($p_{90} = 0.0003$ vs. $p_{10} = 0.07515$ and $p_{50} = 0.07908$) (see *Table 3* and *Figure 18).*

Percentile of Fractional Anisotropy values	*CET*	*Recurrence*	*Edema*	*p-value Edema vs. Recurrence*
Free-Water Corrected DTI data				
10th	0.19191	0.19270	0.24735	**0.00112**
50th	0.35545	0.36701	0.42509	**0.00314**
Mean				**0.0029**
90th	0.52599	0.53314	0.63188	**0.00007**

Original DTI data				
10th	0.07418	0.08654	0.08907	0.07515
50th	0.15967	0.17141	0.01719	0.07908
Mean				0.06146
90th	0.27801	0.26958	0.33056	**0.00030**

Table 3 *- Comparison of different percentiles and mean of FA values between contrast-enhancing tumor (CET), edema with later tumor recurrence and pure peritumoral edema with and without free-water correction.*

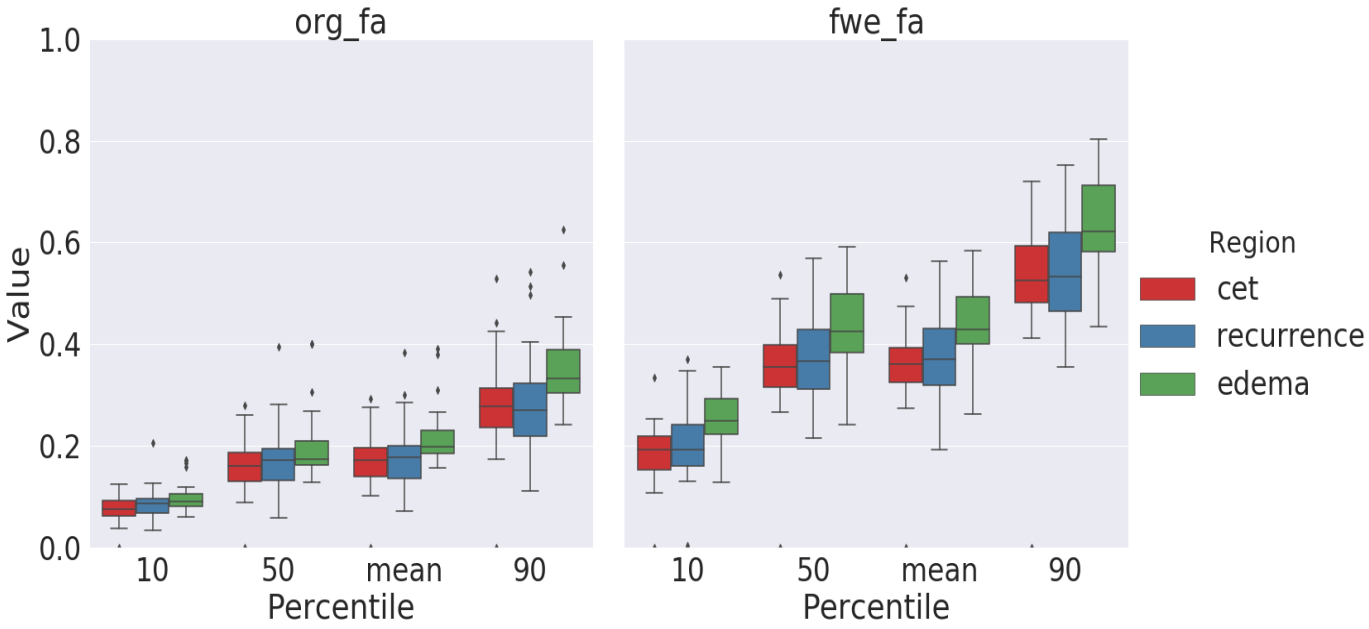

Figure 18 *- Original FA values (left) and FA values after free-water correction (right) comparing contrast-enhancing tumor (red), edema showing later tumor recurrence (blue) and pure edema (green), each for 10th, 50th, and 90th percentile and mean. Diamonds denote outliers.*

4.4 Predictive Value of Free-Water Corrected Fractional Anisotropy Maps

For statistical analysis of the potential of FA maps to predict later tumor recurrence three generalized mixed-effects models were fitted with either noncorrected or FWC FA values or both. The resulting ROC curves can be seen in *Figure 19.*

The cross-validated area under curve (AUC) for FWC FA values was significantly higher than the AUC for a model based on noncorrected FA values (AUC_{FWC} = 0.9 vs. AUC_{org} = 0.77; $p < 0.001$, DeLong's test). This indicates the opportunity to utilize FWC FA maps for prediction of tumor recurrence that is not possible with original, noncorrected FA data.

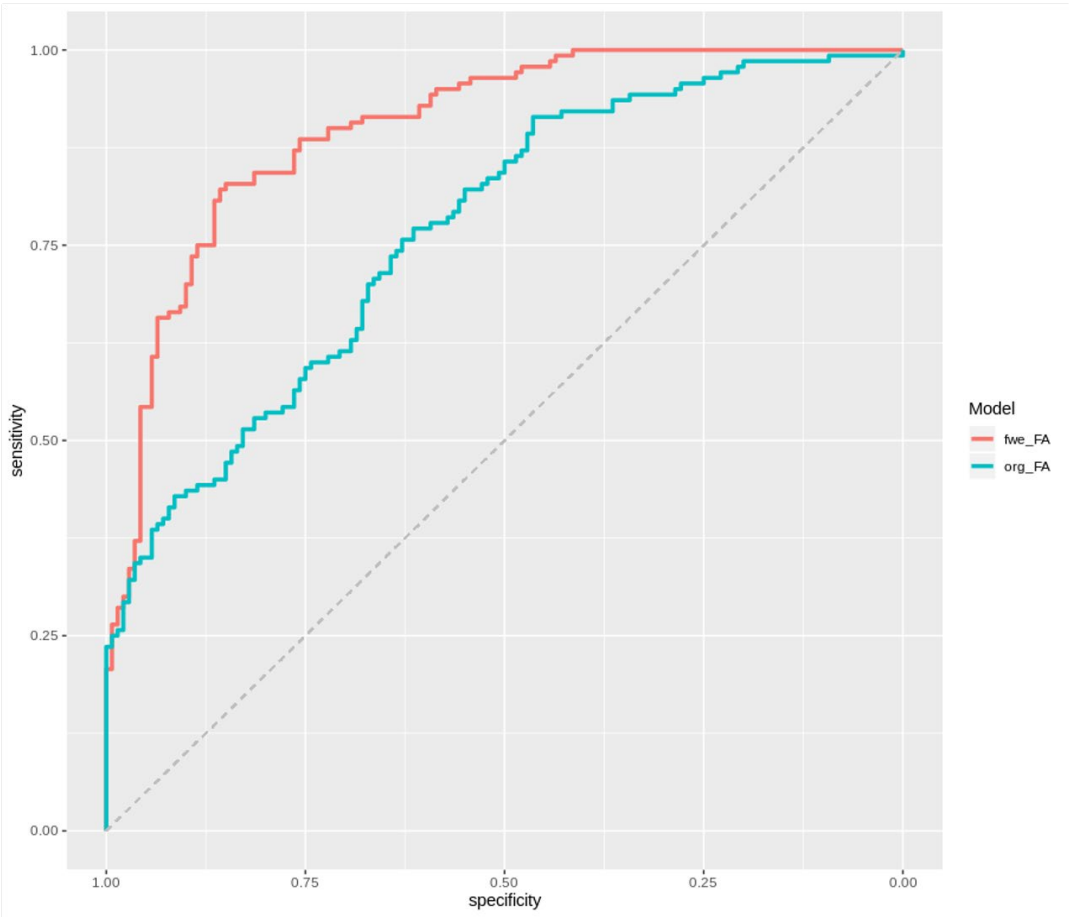

Figure 19 *- Receiver-operating-characteristic curves for a generalized mixed-effect model to predict later recurrence on the basis of free-water corrected FA values (red curve; AUC = 0.9) or noncorrected FA values (turquoise curve; AUC = 0.77). Both models were threefold cross-validated.*

5 Discussion

5.1 Purpose of the Study and Justification of the Methodology

The purpose of our work was to introduce a novel approach for assessing the peritumoral edema of glioblastomas for signal alterations caused by tumor infiltration. By removing the signal of free-water from DTI data we aimed to recover information from the true diffusion signal of the underlying tissue. We were particularly interested in those parts of the preoperative peritumoral edema where later, postoperative images revealed recurrence of the tumor. Our overall goal hereby was to find new and reliable means for recurrence prediction, thereby obtaining valuable information for personalized treatment decisions. Ultimately, we aim to contribute to personalized therapy, thus improving survival times for patients diagnosed with GBM which to date still carries one of the most fatal prognoses of all types of cancer.

Our results demonstrated that free-water corrected FA maps can reveal more pronounced differences between areas with later tumor recurrence and pure, recurrence-free edema. Thus, areas of later tumor recurrence displayed significantly lower FA values, comparable to FA values seen in contrast-enhancing tumor. Those differences were significant even in the lowest range of FA values, whereas uncorrected FA data only showed significant differences in the 90^{th} percentile of FA values. In contrast to that, MD values did not exhibit significant differences between both "types" of peritumoral edema, whether FWC was applied or not. Likewise, the ANN's tissue volume estimates did not show any significant alterations in those parts of the edema where later recurrence appeared.

The reason we applied FWC was to remove the diffusion-isotropic noise stemming from free-water from the diffusion signal with the result of revealing actual tissue anisotropy. We hypothesized that the FA would further decrease in areas of tumor infiltration due to disruption of white matter tracts which would be in accordance with prior studies [80].

We used a two-compartment tissue model to disentangle the true diffusion signal from free-water contamination by modeling the diffusion signal of each single voxel as the contribution of a tissue and a free-water component. Therefore, for the first time, we trained an ANN to estimate the tissue volume fractions directly from the diffusion data. The training set for the model consisted of synthetic, random data on which free-water contamination was induced. There are three benefits of using random data: First, large amounts of data are available without the need of patient data for training. Second, the data is robust against artifacts in the signal.

And third, no assumptions can be made on tissue orientation regarding the prescribed diffusion gradients.

5.2 Comparison with Similar Studies Focusing on Diffusion Tensor Imaging

Our work built on previous studies that examined the peritumoral edema for predicting tumor recurrence. Most related to our work is the study by Bette et al. which also found lower FA values in areas of later tumor recurrence inside the peritumoral edema [79]. In their work, manually drawn regions of interest (ROIs) were placed in the contralateral hemisphere to consider regional differences and obtain comparable FA ratio values. As opposed to that, we used automated tumor segmentation and nonlinear image registration which allowed for an unbiased analysis of the entire peritumoral edema, thus promising higher robustness compared to manual ROI placement. Beyond that, our method can be integrated into fully automated analysis workflows. To objectively evaluate our results in comparison to prior reports, we analyzed them in mixed-effect models. While Bette et al. described an AUC of 0.839 for manually sampled FA values [79], we reported a very similar performance for our automated FWC FA values with an AUC of 0.9, indicating a comparable effectiveness while showing the above-mentioned advantages in methodology.

There are numerous other studies that focused on differentiating peritumoral edema from microscopic glioma infiltration. DTI is a promising, yet controversial tool for these efforts because it assesses local white matter integrity, and FA values have been shown to correlate with cell density and proliferation activity in gliomas [6]. However, utilizing DTI for this purpose is not simple and conflicting results between different studies indicate that there are some limitations and pitfalls to be considered. First, it is noticeable that FA values show a wide heterogeneity, even in healthy brain tissue [81]. Regarding gliomas, one theory states that this diversity is due to multipotent stem cell-like tumor cells which serve as the origin of glial neoplasms. The theory assumes that regional variations in the tumor karyotype develop when the multipotent progenitor cell transforms [82]. This may lead to significant tissue heterogeneity within the tumor. Therefore, Hoefnagels et al. pointed out that FA values have to be assessed locally as he noticed that studies failed to reveal regions of tumor infiltration when they evaluated DTI measurements on a global, only ROI-based level [4]. They thus established a voxel-based probability map based on a combination of DTI parameters to prospectively discern areas of tumor infiltration from vasogenic edema in the same T2-hyperintense region in GBM. As stated above, we also preferred a ROI-free approach for similar reasons and even

found a way to utilize a single DTI parameter (FA) instead of performing a multiparametric assessment.

The tissue heterogeneity might also be the cause why we did not observe significant differences in the recurrence-part of peritumoral edema in the TVMs generated by our ANN, simply because the tissue volume fractions there might be too similar to tissue-rich voxels in the non-recurrence part. Apparently, a few infiltrating tumor cells are enough to alter the FA but they are not reflected in significant differences of the tissue volume estimates immediately.

A second limitation of many DTI-related studies on tumor infiltration is their lack of histopathological verification since in clinical practice, biopsies are usually taken only from the contrast-enhancing part of the tumor. Only a few studies performed stereotactic biopsies of non-enhancing portions of the tumor to investigate correlations between imaging and histopathological parameters in assessing tumor infiltration. However, histopathological verification carries its own risks, for example the potential for misregistration between biopsy sites and MRI findings and the hazard of damaging functioning brain.

Nevertheless, in 2006, Stadlbauer et al. reported a strong, negative correlation between FA and tumor infiltration by histopathological comparison [6]. Unfortunately, they only investigated WHO grade 2 and 3 gliomas, and no GBM were included. Barajas et al. found an inverse correlation between ADC values and cellular proliferation and architectural disruption in non-enhancing regions of GBM when matching DWI findings with histopathological analyses [63]. Although this correlation has been well-established, later studies found that FA is a stronger predictor for tumor cell density than ADC [83]. We therefore focused our work on FA values but also evaluated FWC MD values and our generated TVM.

As regards MD values, here, FWC did not reveal additional information about the microstructure of peritumoral edema. Moreover, due to the removal of the free-water component, which is basically the source of contrast in MD, the signal intensity of the FWC MD values was much lower. The decreased contrast in the FWC MD maps was clearly visible (see *Figure 14).* Therefore, we propose that different methods of DTI processing might be more suitable for the utilization of MD values in this context. Since, as mentioned above [63], ADC maps showed potential in detecting tumor infiltration inside the peritumoral edema and recent studies even successfully evaluated these changes for recurrence prediction [84], more research should be undertaken to detect further potential of MD for this purpose. It should be mentioned here that MD and ADC are not equivalent since they arise from different MRI modalities (DTI vs. DWI) and are calculated in different ways (see *Section 2.1*). However, they both express the

overall magnitude of diffusion in a single voxel (without any directional information) and thus can be interchangeably utilized for similar questions.

Beyond FA and MD, studies have also suggested other DTI parameters in the evaluation of tumor infiltration. Price et al. found that tumor recurrence occurred along directions where the region of abnormal isotropic diffusion *p* extended beyond the region of abnormal anisotropic diffusion *q* [85]. Those examinations on growth patterns warrant further studies on their potential for recurrence prediction as well. Radial and axial diffusivity are further DTI parameters that have already been taken into consideration [86].

5.3 Different Approaches for the Assessment of Tumor Infiltration

In our study on recurrence prediction, we exclusively focused on DTI metrics of the peritumoral edema. However, there have been some other, promising approaches for the assessment of tumor infiltration that used other advanced imaging tools.

Most prominently, amino acid PET has emerged as a possibly useful method for evaluating tumor infiltration, since it has been shown that tracer accumulation of ^{11}C-labeled methionine correlates with tumor cell density within the tumor core of glioma [87]. Yet, background uptake of the tracer makes it more difficult to quantify tumor cell invasion in the surrounding tissue and more advanced methods have to be applied to solve this issue, for example by uncovering the true ^{11}C-methionine uptake by tumor cells via comparison with the ^{18}F-FDG uptake of the same area [88]. More recently, Lundemann et al. reported that ^{18}F-FET-uptake was the most important parameter for their recurrence probability modelling, indicating the relevance of this PET-tracer [89]. Furthermore, ^{18}F-FET-uptake has already been applied for investigating more accurate radiotherapy plans [90].

A recent study of our working group found a correlation between ^{18}F-FET uptake and cellularity in stereotactic biopsies [91]. However, the association with cellularity was even stronger for another, relatively novel MRI technique, namely amide proton transfer-weighted (APT) imaging. Very shortly, APT semi-quantitatively reflects the concentration of endogenous proteins and peptides. It can be measured as the amount of water signal suppression that is caused by chemical exchange of the priorly absorbed energy from macromolecules (received by a selectively applied “off-resonance” radiofrequency-pulse) to the water resonance. APT has already been successfully applied for differentiating between gliomas of different WHO grades [92] and has proved potential in identifying pseudoprogression [93]. Prior studies on the tissue heterogeneity of gliomas exposed by APT [94] and the aforementioned, recent detection of the

correlation with cellularity warrant further studies in the direction of recurrence prediction as well.

Another approach in assessing the peritumoral edema is PWI because studies have shown that, in contrast to the surrounding edema of brain metastases, the peritumoral edema of GBM had significantly higher rCBF values [95]. This is probably due to tumor cell invasion and structural defects in endothelial tight junctions around GBM and carries potential for future studies on recurrence prediction. The above-mentioned study of Lundemann et al. already observed an elevation of vascular permeability (K_i) and extra-cellular blood volume (V_e) for voxels that later showed tumor recurrence [89]. Moreover, it has been reported that patients with a high rCBV on DSC imaging have a significantly more rapid time to progression, independent of pathologic findings [96].

Furthermore, as discussed earlier (see *Section 2.3*), MRS has been used to assess the degree of tumor infiltration, especially in differentiating gliomas from metastases. Generally, studies concluded that NAA concentration is the most significant parameter to detect low levels of tumor cell infiltration [97]. More recently, Anwar et al. found that the amount of cell turnover, as indicated by an elevated Cho/NAA index, was the greatest predictor for the likelihood of a voxel to progress from normal appearing tissue on conventional MRI to non-enhancing tumor [98]. Other studies confirmed these results [99].

Nevertheless, DTI has some important advantages over other advanced imaging methods. In comparison to PET, MRS and PWI, it displays a much better spatial resolution, requires a modest acquisition time and is more broadly available.

However, irrespective of their availability, combinations of these modalities have shown the most promising results in recurrence prediction and future studies should also focus on multiparametric approaches. Recent multiparametric models for recurrence prediction reached AUCs of 0.77 [89] and 0.84 [86]. In the latter study by Akbari et al. it was clearly pointed out that the single MRI parameters each displayed subtle differences between recurrence and non-recurrence but they were not useful for prediction when used individually. However, the integration of the different signals via ML methods provided fairly reliable predictive indices of infiltration and recurrence [86].

Lastly, another approach in estimating future tumor recurrence is the mathematical modeling of tumor growth on the basis of estimated tumor cell density [100]. Based on high resolution MRI scans and FET-PET metabolic maps, this has already been successfully implemented in personalized radiotherapy design [101].

5.4 Clinical Relevance of the Study

The clinical relevance of our study arises from the necessity for a more differentiated assessment of the peritumoral edema. Since GBM are diffusely infiltrating tumors it is a widely accepted fact that the contrast enhancing tumor margins do not represent the true tumor borders [102]. However, due to a lack of methods visualizing this infiltration of the tumor, current surgical treatment of GBM is largely guided by contrast enhancement on T1w MRI. Yet, it is known that this practice leaves the majority of infiltrating tumor unresected. Likewise, the CTV of radiotherapy comprises a mostly uniform margin around the resection bed and recurrence almost always occurs within this peritumoral tissue. Undoubtedly, the efficacy of these therapies could be significantly improved if the exact extent of the infiltrative component within the peritumoral edema was known and could be specifically targeted. Therefore, by providing a new approach for predicting areas beyond the contrast enhancing tumor that are prone to recurrence, we aim to inform more accurate surgery planning and also give guidance for the creation of personalized radiotherapy plans that spare more healthy tissue and allow for dose escalation in the tissue at risk for recurrence. At our institution, Peeken et al. already made a proposition for a novel clinical target volume (nCTV) that is based on *infiltrative GTV (*iGTV*)* added to the current standard GTV of radiotherapy planning (see *Section 2.2.5).* The iGTV here derived from FWC TVM and FA maps and might represent infiltrative tumor within the FLAIR- hyperintense region. They demonstrated that tumor recurrence overlapped with the iGTV and was completely covered by nCTV. Future studies should further assess the true value of iGTV which might benefit from our investigation on FWC FA maps for recurrence prediction.

5.5 Limitations of the Study

Up to now we only performed a retrospective, yet promising analysis of the data. Future studies have to test if simple thresholding of FWC FA data or multiparametric approaches incorporating this and other parameters can reliably identify tumor-infiltrated areas in the peritumoral edema. In a next step, those values should be evaluated in a prospective study.

Another limitation of our study is that it was conducted in a single center with a relatively small number of patients. We expect that the ANN could be applied to DTI data from different centers with comparable performance, but this needs to be demonstrated in future multicenter studies.

Furthermore, to independently validate our results, a histopathological correlation will be beneficial in case further results will allow for extended resection.

Ultimately, deep learning-based correction of diffusion imaging data for free-water contamination holds potential for further applications beyond recurrence prediction of brain tumors. Recently, Weninger et al. introduced their implementation for the improvement of peritumoral tractography which might be relevant for presurgical planning [103]. This is just another piece of evidence indicating that FWC needs to be taken into consideration whenever areas of the brain need to be assessed that exhibit partial volume effects and might benefit from the differentiation of the free-water and tissue component.

6 Conclusion and Future Directions

It has become clear that conventional T1w- / T2w images are insufficient for assessing the invasion of GBM into their surrounding tissue. Developing means to improve the detection of tumor infiltration in the peritumoral edema to guide more accurate surgery planning and personalized radiotherapy plans plays a key role in combating the fatal prognosis of this tumor entity. To date, none of the numerous approaches for challenging this issue has been transferred to clinical practice.

The elimination of the free-water contamination of DTI data using an ANN has emerged as a promising, new method for predicting the areas of the peritumoral edema where later recurrence occurred: FWC FA values differed significantly between areas of later tumor recurrence and pure, vasogenic edema. Due to the fact that this analysis has been performed on preoperative and widely applicable MR data, it carries the potential to be utilized for personalized surgical and radiation therapy planning in the future.

Further studies need to prove its capability to be applied prospectively and its applicability in different centers and on larger patient cohorts.

This work highlights the potential of *artificial intelligence* (AI) - driven image analysis in neuroradiology. It may be expected that future developments in this field will eventually lead to improved outcome of patients diagnosed with malignant brain tumors. The application of AI might help to uncover more useful information from imaging data by finding patterns in large amounts of data, providing powerful image processing tools and enabling future methods that have not been thought up before and remain with the reader's imagination.

In conclusion, rather than being a threat, AI emerges as an exciting tool for the neuroradiologist to enhance brain tumor imaging and enlivens further research in this field.

7 Abbreviations

ADC:	Apparent Diffusion Coefficient
AI:	Artificial Intelligence
ANN:	Artificial Neural Network
APT:	Amide Proton Transfer
a.u.:	Arbitrary unit
AUC:	Area under Curve
CE-T1w:	Contrast-enhanced T1-weighted MRI sequence
Cho:	Choline
CNS:	Central Nervous System
CSF:	Cerebrospinal Fluid
CT:	Computed Tomography
CTV:	Clinical Target Volume
D:	Diffusion
DCE:	Dynamic Contrast Enhancement
DL:	Deep Learning
DSC:	Dynamic Susceptibility Contrast
DTI:	Diffusion Tensor Imaging
DWI:	Diffusion Weighted Imaging
EORTC:	European Organization for Research and Treatment of Cancer
EPI:	Echoplanar Imaging
FA:	Fractional Anisotropy
FDG:	Fluordeoxyglucose
FET:	Fluoroethyltyrosine
FLAIR:	Fluid Attenuated Inversion Recovery
fMRI:	Functional Magnetic Resonance Imaging
FWC:	Free Water Correction
FWE:	Free Water Elimination
GBM:	Glioblastoma (glioblastoma multiforme)
GRE:	Gradient Recalled Echo
GTV:	Gross Tumor Volume
IDH:	Isocitrate dehydrogenase
iGTV:	Infiltrative Gross Tumor Volume

KPS: Karnofsky Performance Score

MD: Mean Diffusivity

MGMT: O^6-methylguanine-DNA methyltransferase

ML: Machine Learning

MOS: Median Overall Survival

MRI: Magnetic Resonance Imaging

MRS: Magnetic Resonance Spectroscopy

NAA: N-acetylaspartate

NOS: Not otherwise specified

nGTV: Novel Clinical Target Volume

PET: Positron Emission Tomography

PFS: Progression Free Survival

PTV: Planning target volume

PWI: Perfusion Weighted Imaging

RANO: Response Assessment in Neuro-Oncology

rCBF: Relative Cerebral Blood Flow

ROC: Receiver Operating Characteristic

ROI: Region of Interest

RTOG: Radiotherapy and Oncology Group

SE: Spin Echo

SNR: Signal-to-Noise Ratio

T1w: T1-weighted sequence

T2w: T2-weighted sequence

TTF: Tumor-treating fields

TVM: Tissue volume maps

VEGF: Vascular Endothelial Growth Factor

WHO: World Health Organization

8 List of Figures

9 List of Tables

10 Bibliography

[1] L. Marenco-Hillembrand *et al.*, “Trends in glioblastoma: outcomes over time and type of intervention: a systematic evidence based analysis,” *J Neurooncol*, vol. 147, no. 2, pp. 297–307, Apr. 2020, doi: 10.1007/s11060-020-03451-6.

[2] M. Weller, T. Cloughesy, J. R. Perry, and W. Wick, “Standards of care for treatment of recurrent glioblastoma—are we there yet?,” *Neuro Oncol*, vol. 15, no. 1, pp. 4–27, Jan. 2013, doi: 10.1093/neuonc/nos273.

[3] S. Bette *et al.*, “Retrospective Analysis of Radiological Recurrence Patterns in Glioblastoma, Their Prognostic Value And Association to Postoperative Infarct Volume,” *Sci Rep*, vol. 8, no. 1, p. 4561, Mar. 2018, doi: 10.1038/s41598-018-22697-9.

[4] F. W. A. Hoefnagels *et al.*, “Differentiation of edema and glioma infiltration: proposal of a DTI-based probability map,” *J Neurooncol*, vol. 120, no. 1, pp. 187–198, Oct. 2014, doi: 10.1007/s11060-014-1544-9.

[5] O. Pasternak, N. Sochen, Y. Gur, N. Intrator, and Y. Assaf, “Free water elimination and mapping from diffusion MRI,” *Magnetic Resonance in Medicine*, vol. 62, no. 3, pp. 717–730, Sep. 2009, doi: 10.1002/mrm.22055.

[6] A. Stadlbauer *et al.*, “Gliomas: histopathologic evaluation of changes in directionality and magnitude of water diffusion at diffusion-tensor MR imaging,” *Radiology*, vol. 240, no. 3, pp. 803–810, Sep. 2006, doi: 10.1148/radiol.2403050937.

[7] M. Molina-Romero, B. Wiestler, P. A. Gómez, M. I. Menzel, and B. H. Menze, “Deep Learning with Synthetic Diffusion MRI Data for Free-Water Elimination in Glioblastoma Cases,” in *Medical Image Computing and Computer Assisted Intervention – MICCAI 2018*, 2018, pp. 98–106.

[8] D. Le Bihan, E. Breton, D. Lallemand, P. Grenier, E. Cabanis, and M. Laval-Jeantet, “MR imaging of intravoxel incoherent motions: application to diffusion and perfusion in neurologic disorders,” *Radiology*, vol. 161, no. 2, pp. 401–407, Nov. 1986, doi: 10.1148/radiology.161.2.3763909.

[9] M. K. Stehling, R. Turner, and P. Mansfield, “Echo-planar imaging: magnetic resonance imaging in a fraction of a second,” *Science*, vol. 254, no. 5028, pp. 43–50, Oct. 1991, doi: 10.1126/science.1925560.

[10] E. R. Melhem, S. Mori, G. Mukundan, M. A. Kraut, M. G. Pomper, and P. C. M. van Zijl, “Diffusion Tensor MR Imaging of the Brain and White Matter Tractography,” *American Journal of Roentgenology*, vol. 178, no. 1, pp. 3–16, Jan. 2002, doi: 10.2214/ajr.178.1.1780003.

[11] M. L. Lipton, “Diffusion: Detection of Microscopic Motion,” in *Totally Accessible MRI: A User’s Guide to Principles, Technology, and Applications*, M. L. Lipton, Ed. New York, NY: Springer, 2008, pp. 233–244. doi: 10.1007/978-0-387-48896-7_17.

[12] P. J. Basser, J. Mattiello, and D. LeBihan, “MR diffusion tensor spectroscopy and imaging,” *Biophys J*, vol. 66, no. 1, pp. 259–267, Jan. 1994, doi: 10.1016/S0006-3495(94)80775-1.

[13] B. J. Jellison, A. S. Field, J. Medow, M. Lazar, M. S. Salamat, and A. L. Alexander, “Diffusion Tensor Imaging of Cerebral White Matter: A Pictorial Review of Physics, Fiber Tract Anatomy, and Tumor Imaging Patterns,” p. 14, 2004.

[14] D. K. Jones, “The effect of gradient sampling schemes on measures derived from diffusion tensor MRI: a Monte Carlo study,” *Magn Reson Med*, vol. 51, no. 4, pp. 807–815, Apr. 2004, doi: 10.1002/mrm.20033.

[15] S. Pajevic and C. Pierpaoli, “Color schemes to represent the orientation of anisotropic tissues from diffusion tensor data: application to white matter fiber tract mapping in the human brain,” *Magn Reson Med*, vol. 42, no. 3, pp. 526–540, Sep. 1999.

[16] J. Soares, P. Marques, V. Alves, and N. Sousa, “A hitchhiker’s guide to diffusion tensor imaging,” *Front. Neurosci.*, vol. 7, 2013, doi: 10.3389/fnins.2013.00031.
[17] L. R. Ranzenberger and T. Snyder, “Diffusion Tensor Imaging,” in *StatPearls*, Treasure Island (FL): StatPearls Publishing, 2020. Accessed: Feb. 13, 2021. [Online]. Available: http://www.ncbi.nlm.nih.gov/books/NBK537361/
[18] R. Stupp *et al.*, “Radiotherapy plus concomitant and adjuvant temozolomide for glioblastoma,” *N Engl J Med*, vol. 352, no. 10, pp. 987–996, Mar. 2005, doi: 10.1056/NEJMoa043330.
[19] M. Weller *et al.*, “European Association for Neuro-Oncology (EANO) guideline on the diagnosis and treatment of adult astrocytic and oligodendroglial gliomas,” *Lancet Oncol.*, vol. 18, no. 6, pp. e315–e329, 2017, doi: 10.1016/S1470-2045(17)30194-8.
[20] K. Kraywinkel and C. Spix, “Epidemiologie primärer Hirntumoren bei Kindern und Erwachsenen in Deutschland,” *Der Onkologe*, vol. 25, no. 1, pp. 5–9, Jan. 2019, doi: 10.1007/s00761-018-0501-1.
[21] M. Wrensch, Y. Minn, T. Chew, M. Bondy, and M. S. Berger, “Epidemiology of primary brain tumors: current concepts and review of the literature,” *Neuro Oncol*, vol. 4, no. 4, pp. 278–299, Oct. 2002, doi: 10.1093/neuonc/4.4.278.
[22] D. T. Blumenthal and L. A. Cannon-Albright, “Familiality in brain tumors,” *Neurology*, vol. 71, no. 13, pp. 1015–1020, Sep. 2008, doi: 10.1212/01.wnl.0000326597.60605.27.
[23] N. Savage, “Searching for the roots of brain cancer,” *Nature*, vol. 561, no. 7724, Art. no. 7724, Sep. 2018, doi: 10.1038/d41586-018-06709-2.
[24] D. N. Louis *et al.*, “The 2016 World Health Organization Classification of Tumors of the Central Nervous System: a summary,” *Acta Neuropathol.*, vol. 131, no. 6, pp. 803–820, 2016, doi: 10.1007/s00401-016-1545-1.
[25] J. C. DeWitt, A. Mock, and D. N. Louis, “The 2016 WHO classification of central nervous system tumors: what neurologists need to know,” *Curr Opin Neurol*, vol. 30, no. 6, pp. 643–649, Dec. 2017, doi: 10.1097/WCO.0000000000000490.
[26] H. Ohgaki and P. Kleihues, “The definition of primary and secondary glioblastoma,” *Clin Cancer Res*, vol. 19, no. 4, pp. 764–772, Feb. 2013, doi: 10.1158/1078-0432.CCR-12-3002.
[27] W. Stummer *et al.*, “Fluorescence-guided surgery with 5-aminolevulinic acid for resection of malignant glioma: a randomised controlled multicentre phase III trial,” *Lancet Oncol*, vol. 7, no. 5, pp. 392–401, May 2006, doi: 10.1016/S1470-2045(06)70665-9.
[28] N. Laperriere, L. Zuraw, G. Cairncross, and Cancer Care Ontario Practice Guidelines Initiative Neuro-Oncology Disease Site Group, “Radiotherapy for newly diagnosed malignant glioma in adults: a systematic review,” *Radiother Oncol*, vol. 64, no. 3, pp. 259–273, Sep. 2002, doi: 10.1016/s0167-8140(02)00078-6.
[29] S. N. Badiyan *et al.*, “Radiation therapy dose escalation for glioblastoma multiforme in the era of temozolomide,” *Int J Radiat Oncol Biol Phys*, vol. 90, no. 4, pp. 877–885, Nov. 2014, doi: 10.1016/j.ijrobp.2014.07.014.
[30] J. C. Peeken *et al.*, “Deep learning derived tumor infiltration maps for personalized target definition in Glioblastoma radiotherapy,” *Radiother Oncol*, vol. 138, pp. 166–172, Jul. 2019, doi: 10.1016/j.radonc.2019.06.031.
[31] R. Stupp *et al.*, “Cilengitide combined with standard treatment for patients with newly diagnosed glioblastoma with methylated MGMT promoter (CENTRIC EORTC 26071-22072 study): a multicentre, randomised, open-label, phase 3 trial,” *The Lancet Oncology*, vol. 15, no. 10, pp. 1100–1108, Sep. 2014, doi: 10.1016/S1470-2045(14)70379-1.
[32] M. Niyazi *et al.*, “ESTRO-ACROP guideline ‘target delineation of glioblastomas,’” *Radiother Oncol*, vol. 118, no. 1, pp. 35–42, Jan. 2016, doi: 10.1016/j.radonc.2015.12.003.
[33] T. Kazda *et al.*, “Radiotherapy of Glioblastoma 15 Years after the Landmark Stupp’s

Trial: More Controversies than Standards?," *Radiol Oncol*, vol. 52, no. 2, pp. 121–128, Jun. 2018, doi: 10.2478/raon-2018-0023.
[34] P. K. Sneed *et al.*, "Patterns of recurrence of glioblastoma multiforme after external irradiation followed by implant boost," *Int J Radiat Oncol Biol Phys*, vol. 29, no. 4, pp. 719–727, Jul. 1994, doi: 10.1016/0360-3016(94)90559-2.
[35] M. Weller *et al.*, "MGMT Promoter Methylation Is a Strong Prognostic Biomarker for Benefit from Dose-Intensified Temozolomide Rechallenge in Progressive Glioblastoma: The DIRECTOR Trial," *Clin Cancer Res*, vol. 21, no. 9, pp. 2057–2064, May 2015, doi: 10.1158/1078-0432.CCR-14-2737.
[36] K. Seystahl, W. Wick, and M. Weller, "Therapeutic options in recurrent glioblastoma--An update," *Crit Rev Oncol Hematol*, vol. 99, pp. 389–408, Mar. 2016, doi: 10.1016/j.critrevonc.2016.01.018.
[37] W. Wick *et al.*, "EORTC 26101 phase III trial exploring the combination of bevacizumab and lomustine in patients with first progression of a glioblastoma.," *JCO*, vol. 34, no. 15_suppl, pp. 2001–2001, May 2016, doi: 10.1200/JCO.2016.34.15_suppl.2001.
[38] D. R. Johnson, D. J. Ma, J. C. Buckner, and J. E. Hammack, "Conditional probability of long-term survival in glioblastoma: a population-based analysis," *Cancer*, vol. 118, no. 22, pp. 5608–5613, Nov. 2012, doi: 10.1002/cncr.27590.
[39] A. Malmström *et al.*, "Temozolomide versus standard 6-week radiotherapy versus hypofractionated radiotherapy in patients older than 60 years with glioblastoma: the Nordic randomised, phase 3 trial," *Lancet Oncol*, vol. 13, no. 9, pp. 916–926, Sep. 2012, doi: 10.1016/S1470-2045(12)70265-6.
[40] F. M. Iwamoto *et al.*, "Patterns of relapse and prognosis after bevacizumab failure in recurrent glioblastoma," *Neurology*, vol. 73, no. 15, pp. 1200–1206, Oct. 2009, doi: 10.1212/WNL.0b013e3181bc0184.
[41] B. M. Ellingson *et al.*, "Consensus recommendations for a standardized Brain Tumor Imaging Protocol in clinical trials," *Neuro Oncol*, vol. 17, no. 9, pp. 1188–1198, Sep. 2015, doi: 10.1093/neuonc/nov095.
[42] G. Shukla *et al.*, "Advanced magnetic resonance imaging in glioblastoma: a review," *Chin Clin Oncol*, vol. 6, no. 4, p. 40, Aug. 2017, doi: 10.21037/cco.2017.06.28.
[43] E. Y. K. Tsui, J. H. Chan, Y. K. Cheung, K. F. Lai, D. Fong, and S. H. Ng, "Evaluation of cerebral abscesses by diffusion-weighted MR imaging and MR spectroscopy," *Comput Med Imaging Graph*, vol. 26, no. 5, pp. 347–351, Oct. 2002, doi: 10.1016/s0895-6111(02)00018-6.
[44] E. L. Chang *et al.*, "Evaluation of peritumoral edema in the delineation of radiotherapy clinical target volumes for glioblastoma," *Int J Radiat Oncol Biol Phys*, vol. 68, no. 1, pp. 144–150, May 2007, doi: 10.1016/j.ijrobp.2006.12.009.
[45] N. Sanai, Z. Mirzadeh, and M. S. Berger, "Functional outcome after language mapping for glioma resection," *N Engl J Med*, vol. 358, no. 1, pp. 18–27, Jan. 2008, doi: 10.1056/NEJMoa067819.
[46] K. G. Abdullah, D. Lubelski, P. G. P. Nucifora, and S. Brem, "Use of diffusion tensor imaging in glioma resection," *Neurosurg Focus*, vol. 34, no. 4, p. E1, Apr. 2013, doi: 10.3171/2013.1.FOCUS12412.
[47] S.-K. Lee, "Diffusion tensor and perfusion imaging of brain tumors in high-field MR imaging," *Neuroimaging Clin N Am*, vol. 22, no. 2, pp. 123–134, ix, May 2012, doi: 10.1016/j.nic.2012.02.001.
[48] S. Wang *et al.*, "Differentiation between glioblastomas, solitary brain metastases, and primary cerebral lymphomas using diffusion tensor and dynamic susceptibility contrast-enhanced MR imaging," *AJNR Am J Neuroradiol*, vol. 32, no. 3, pp. 507–514, Mar. 2011, doi: 10.3174/ajnr.A2333.
[49] R. Kim *et al.*, "Prognosis prediction of non-enhancing T2 high signal intensity lesions

in glioblastoma patients after standard treatment: application of dynamic contrast-enhanced MR imaging," *Eur Radiol*, vol. 27, no. 3, pp. 1176–1185, Mar. 2017, doi: 10.1007/s00330-016-4464-6.
[50] A. Chakravorty, T. Steel, and J. Chaganti, "Accuracy of percentage of signal intensity recovery and relative cerebral blood volume derived from dynamic susceptibility-weighted, contrast-enhanced MRI in the preoperative diagnosis of cerebral tumours," *Neuroradiol J*, vol. 28, no. 6, pp. 574–583, Dec. 2015, doi: 10.1177/1971400915611916.
[51] A. Horská and P. B. Barker, "Imaging of Brain Tumors: MR Spectroscopy and Metabolic Imaging," *Neuroimaging Clin N Am*, vol. 20, no. 3, pp. 293–310, Aug. 2010, doi: 10.1016/j.nic.2010.04.003.
[52] R. N. Al-Okaili *et al.*, "Intraaxial brain masses: MR imaging-based diagnostic strategy--initial experience," *Radiology*, vol. 243, no. 2, pp. 539–550, May 2007, doi: 10.1148/radiol.2432060493.
[53] H. Nandu, P. Y. Wen, and R. Y. Huang, "Imaging in neuro-oncology," *Ther Adv Neurol Disord*, vol. 11, Feb. 2018, doi: 10.1177/1756286418759865.
[54] P. Lambin *et al.*, "Radiomics: extracting more information from medical images using advanced feature analysis," *Eur J Cancer*, vol. 48, no. 4, pp. 441–446, Mar. 2012, doi: 10.1016/j.ejca.2011.11.036.
[55] B. Wiestler *et al.*, "Multiparametric MRI-based differentiation of WHO grade II/III glioma and WHO grade IV glioblastoma," *Sci Rep*, vol. 6, p. 35142, Oct. 2016, doi: 10.1038/srep35142.
[56] O. C. Andronesi *et al.*, "Detection of oncogenic IDH1 mutations using magnetic resonance spectroscopy of 2-hydroxyglutarate," *J Clin Invest*, vol. 123, no. 9, pp. 3659–3663, Sep. 2013, doi: 10.1172/JCI67229.
[57] A. Verger *et al.*, "Static and dynamic 18F-FET PET for the characterization of gliomas defined by IDH and 1p/19q status," *Eur J Nucl Med Mol Imaging*, vol. 45, no. 3, pp. 443–451, Mar. 2018, doi: 10.1007/s00259-017-3846-6.
[58] B. Zhang *et al.*, "Multimodal MRI features predict isocitrate dehydrogenase genotype in high-grade gliomas," *Neuro Oncol*, vol. 19, no. 1, pp. 109–117, Jan. 2017, doi: 10.1093/neuonc/now121.
[59] P. Eichinger *et al.*, "Diffusion tensor image features predict IDH genotype in newly diagnosed WHO grade II/III gliomas," *Sci Rep*, vol. 7, no. 1, p. 13396, Oct. 2017, doi: 10.1038/s41598-017-13679-4.
[60] P. Y. Wen *et al.*, "Updated response assessment criteria for high-grade gliomas: response assessment in neuro-oncology working group," *J Clin Oncol*, vol. 28, no. 11, pp. 1963–1972, Apr. 2010, doi: 10.1200/JCO.2009.26.3541.
[61] R.-E. Yoo *et al.*, "Independent Poor Prognostic Factors for True Progression after Radiation Therapy and Concomitant Temozolomide in Patients with Glioblastoma: Subependymal Enhancement and Low ADC Value," *AJNR Am J Neuroradiol*, vol. 36, no. 10, pp. 1846–1852, Oct. 2015, doi: 10.3174/ajnr.A4401.
[62] C. Reimer *et al.*, "Differentiation of pseudoprogression and real progression in glioblastoma using ADC parametric response maps," *PLoS One*, vol. 12, no. 4, p. e0174620, 2017, doi: 10.1371/journal.pone.0174620.
[63] R. F. Barajas *et al.*, "Differentiation of recurrent glioblastoma multiforme from radiation necrosis after external beam radiation therapy with dynamic susceptibility-weighted contrast-enhanced perfusion MR imaging," *Radiology*, vol. 253, no. 2, pp. 486–496, Nov. 2009, doi: 10.1148/radiol.2532090007.
[64] N. Galldiks *et al.*, "Diagnosis of pseudoprogression in patients with glioblastoma using O-(2-[18F]fluoroethyl)-L-tyrosine PET," *Eur J Nucl Med Mol Imaging*, vol. 42, no. 5, pp. 685–695, Apr. 2015, doi: 10.1007/s00259-014-2959-4.
[65] H. Zhang, L. Ma, Q. Wang, X. Zheng, C. Wu, and B.-N. Xu, "Role of magnetic

resonance spectroscopy for the differentiation of recurrent glioma from radiation necrosis: a systematic review and meta-analysis," *Eur J Radiol*, vol. 83, no. 12, pp. 2181–2189, Dec. 2014, doi: 10.1016/j.ejrad.2014.09.018.
[66] A. D. Norden *et al.*, "An exploratory survival analysis of anti-angiogenic therapy for recurrent malignant glioma," *J Neurooncol*, vol. 92, no. 2, pp. 149–155, Apr. 2009, doi: 10.1007/s11060-008-9745-8.
[67] B. M. Ellingson *et al.*, "Recurrent glioblastoma treated with bevacizumab: contrast-enhanced T1-weighted subtraction maps improve tumor delineation and aid prediction of survival in a multicenter clinical trial," *Radiology*, vol. 271, no. 1, pp. 200–210, Apr. 2014, doi: 10.1148/radiol.13131305.
[68] H. S. Nguyen *et al.*, "Progressing bevacizumab-induced diffusion restriction is associated with coagulative necrosis surrounded by viable tumor and decreased overall survival in recurrent glioblastoma patients," *AJNR Am J Neuroradiol*, vol. 37, no. 12, pp. 2201–2208, Dec. 2016, doi: 10.3174/ajnr.A4898.
[69] H. Okada *et al.*, "Immunotherapy response assessment in neuro-oncology: a report of the RANO working group," *Lancet Oncol*, vol. 16, no. 15, pp. e534–e542, Nov. 2015, doi: 10.1016/S1470-2045(15)00088-1.
[70] E. J. Alberts, "Multi-modal Multi-temporal Brain Tumor Segmentation, Growth Analysis and Texture-based Classification," p. 153.
[71] P. A. Yushkevich, Y. Gao, and G. Gerig, "ITK-SNAP: an interactive tool for semi-automatic segmentation of multi-modality biomedical images," *Conf Proc IEEE Eng Med Biol Soc*, vol. 2016, pp. 3342–3345, Aug. 2016, doi: 10.1109/EMBC.2016.7591443.
[72] B. B. Avants, N. J. Tustison, G. Song, P. A. Cook, A. Klein, and J. C. Gee, "A reproducible evaluation of ANTs similarity metric performance in brain image registration," *Neuroimage*, vol. 54, no. 3, pp. 2033–2044, Feb. 2011, doi: 10.1016/j.neuroimage.2010.09.025.
[73] M. C. Papadopoulos, S. Saadoun, D. K. Binder, G. T. Manley, S. Krishna, and A. S. Verkman, "Molecular mechanisms of brain tumor edema," *Neuroscience*, vol. 129, no. 4, pp. 1009–1018, Jan. 2004, doi: 10.1016/j.neuroscience.2004.05.044.
[74] C. Pierpaoli and P. J. Basser, "Toward a quantitative assessment of diffusion anisotropy," *Magn Reson Med*, vol. 36, no. 6, pp. 893–906, Dec. 1996, doi: 10.1002/mrm.1910360612.
[75] M.-C. Chou *et al.*, "FLAIR diffusion-tensor MR tractography: comparison of fiber tracking with conventional imaging," *AJNR Am J Neuroradiol*, vol. 26, no. 3, pp. 591–597, Mar. 2005.
[76] A. R. Hoy, C. G. Koay, S. R. Kecskemeti, and A. L. Alexander, "Optimization of a free water elimination two-compartment model for diffusion tensor imaging," *Neuroimage*, vol. 103, pp. 323–333, Dec. 2014, doi: 10.1016/j.neuroimage.2014.09.053.
[77] L.-C. Chang, D. K. Jones, and C. Pierpaoli, "RESTORE: robust estimation of tensors by outlier rejection," *Magn Reson Med*, vol. 53, no. 5, pp. 1088–1095, May 2005, doi: 10.1002/mrm.20426.
[78] M.-C. Metz *et al.*, "Predicting Glioblastoma Recurrence from Preoperative MR Scans Using Fractional-Anisotropy Maps with Free-Water Suppression," *Cancers*, vol. 12, no. 3, Art. no. 3, Mar. 2020, doi: 10.3390/cancers12030728.
[79] S. Bette *et al.*, "Local Fractional Anisotropy Is Reduced in Areas with Tumor Recurrence in Glioblastoma," *Radiology*, vol. 283, no. 2, pp. 499–507, May 2017, doi: 10.1148/radiol.2016152832.
[80] C. R. Durst *et al.*, "Multimodal MR imaging model to predict tumor infiltration in patients with gliomas," *Neuroradiology*, vol. 56, no. 2, pp. 107–115, Feb. 2014, doi: 10.1007/s00234-013-1308-9.
[81] X. Kang, T. J. Herron, and D. L. Woods, "Regional variation, hemispheric

asymmetries and gender differences in pericortical white matter," *Neuroimage*, vol. 56, no. 4, pp. 2011–2023, Jun. 2011, doi: 10.1016/j.neuroimage.2011.03.016.
[82] N. Sanai, A. Alvarez-Buylla, and M. S. Berger, "Neural stem cells and the origin of gliomas," *N Engl J Med*, vol. 353, no. 8, pp. 811–822, Aug. 2005, doi: 10.1056/NEJMra043666.
[83] E. D. H. Gates *et al.*, "Estimating Local Cellular Density in Glioma Using MR Imaging Data," *American Journal of Neuroradiology*, vol. 42, no. 1, pp. 102–108, Jan. 2021, doi: 10.3174/ajnr.A6884.
[84] P. D. Chang, D. S. Chow, P. H. Yang, C. G. Filippi, and A. Lignelli, "Predicting Glioblastoma Recurrence by Early Changes in the Apparent Diffusion Coefficient Value and Signal Intensity on FLAIR Images," *American Journal of Roentgenology*, vol. 208, no. 1, pp. 57–65, Oct. 2016, doi: 10.2214/AJR.16.16234.
[85] S. J. Price, R. Jena, N. G. Burnet, T. A. Carpenter, J. D. Pickard, and J. H. Gillard, "Predicting patterns of glioma recurrence using diffusion tensor imaging," *Eur Radiol*, vol. 17, no. 7, pp. 1675–1684, Jul. 2007, doi: 10.1007/s00330-006-0561-2.
[86] H. Akbari *et al.*, "Imaging Surrogates of Infiltration Obtained Via Multiparametric Imaging Pattern Analysis Predict Subsequent Location of Recurrence of Glioblastoma," *Neurosurgery*, vol. 78, no. 4, pp. 572–580, Apr. 2016, doi: 10.1227/NEU.0000000000001202.
[87] Y. Okita *et al.*, "(11)C-methionine uptake correlates with tumor cell density rather than with microvessel density in glioma: A stereotactic image-histology comparison," *Neuroimage*, vol. 49, no. 4, pp. 2977–2982, Feb. 2010, doi: 10.1016/j.neuroimage.2009.11.024.
[88] M. Kinoshita *et al.*, "A novel PET index, 18F-FDG-11C-methionine uptake decoupling score, reflects glioma cell infiltration," *J Nucl Med*, vol. 53, no. 11, pp. 1701–1708, Nov. 2012, doi: 10.2967/jnumed.112.104992.
[89] M. Lundemann *et al.*, "Feasibility of multi-parametric PET and MRI for prediction of tumour recurrence in patients with glioblastoma," *Eur. J. Nucl. Med. Mol. Imaging*, vol. 46, no. 3, pp. 603–613, 2019, doi: 10.1007/s00259-018-4180-3.
[90] M. Harat, B. Małkowski, and R. Makarewicz, "Pre-irradiation tumour volumes defined by MRI and dual time-point FET-PET for the prediction of glioblastoma multiforme recurrence: A prospective study," *Radiotherapy and Oncology*, vol. 120, no. 2, pp. 241–247, Aug. 2016, doi: 10.1016/j.radonc.2016.06.004.
[91] S. Schön *et al.*, "Imaging glioma biology: spatial comparison of amino acid PET, amide proton transfer, and perfusion-weighted MRI in newly diagnosed gliomas," *Eur J Nucl Med Mol Imaging*, vol. 47, no. 6, pp. 1468–1475, Jun. 2020, doi: 10.1007/s00259-019-04677-x.
[92] Y. S. Choi *et al.*, "Amide proton transfer imaging to discriminate between low- and high-grade gliomas: added value to apparent diffusion coefficient and relative cerebral blood volume," *Eur Radiol*, vol. 27, no. 8, pp. 3181–3189, Aug. 2017, doi: 10.1007/s00330-017-4732-0.
[93] S. Jiang *et al.*, "Identifying Recurrent Malignant Glioma after Treatment Using Amide Proton Transfer-Weighted MR Imaging: A Validation Study with Image-Guided Stereotactic Biopsy," *Clin Cancer Res*, vol. 25, no. 2, pp. 552–561, Jan. 2019, doi: 10.1158/1078-0432.CCR-18-1233.
[94] Z. Wen *et al.*, "MR imaging of high-grade brain tumors using endogenous protein and peptide-based contrast," *Neuroimage*, vol. 51, no. 2, pp. 616–622, Jun. 2010, doi: 10.1016/j.neuroimage.2010.02.050.
[95] A. Server, T. E. D. Orheim, B. A. Graff, R. Josefsen, T. Kumar, and P. H. Nakstad, "Diagnostic examination performance by using microvascular leakage, cerebral blood volume, and blood flow derived from 3-T dynamic susceptibility-weighted contrast-enhanced

perfusion MR imaging in the differentiation of glioblastoma multiforme and brain metastasis," *Neuroradiology*, vol. 53, no. 5, pp. 319–330, May 2011, doi: 10.1007/s00234-010-0740-3.
[96] M. Law *et al.*, "Gliomas: predicting time to progression or survival with cerebral blood volume measurements at dynamic susceptibility-weighted contrast-enhanced perfusion MR imaging," *Radiology*, vol. 247, no. 2, pp. 490–498, May 2008, doi: 10.1148/radiol.2472070898.
[97] A. Stadlbauer *et al.*, "Proton magnetic resonance spectroscopic imaging in the border zone of gliomas: correlation of metabolic and histological changes at low tumor infiltration--initial results," *Invest Radiol*, vol. 42, no. 4, pp. 218–223, Apr. 2007, doi: 10.1097/01.rli.0000255812.61435.67.
[98] M. Anwar *et al.*, "Identifying Voxels at Risk for Progression in Glioblastoma Based on Dosimetry, Physiologic and Metabolic MRI," *Radiat Res*, vol. 188, no. 3, pp. 303–313, Sep. 2017, doi: 10.1667/RR14662.1.
[99] Y. Cui *et al.*, "Higher Cho/NAA Ratio in Postoperative Peritumoral Edema Zone Is Associated With Earlier Recurrence of Glioblastoma," *Front Neurol*, vol. 11, p. 592155, 2020, doi: 10.3389/fneur.2020.592155.
[100] J. Unkelbach, B. H. Menze, E. Konukoglu, F. Dittmann, N. Ayache, and H. A. Shih, "Radiotherapy planning for glioblastoma based on a tumor growth model: implications for spatial dose redistribution," *Phys. Med. Biol.*, vol. 59, no. 3, pp. 771–789, Jan. 2014, doi: 10.1088/0031-9155/59/3/771.
[101] J. Lipkova *et al.*, "Personalized Radiotherapy Design for Glioblastoma: Integrating Mathematical Tumor Models, Multimodal Scans, and Bayesian Inference," *IEEE Trans Med Imaging*, vol. 38, no. 8, pp. 1875–1884, Aug. 2019, doi: 10.1109/TMI.2019.2902044.
[102] S. Lu, D. Ahn, G. Johnson, M. Law, D. Zagzag, and R. I. Grossman, "Diffusion-tensor MR imaging of intracranial neoplasia and associated peritumoral edema: introduction of the tumor infiltration index," *Radiology*, vol. 232, no. 1, pp. 221–228, Jul. 2004, doi: 10.1148/radiol.2321030653.
[103] L. Weninger, C.-H. Na, K. Jütten, and D. Merhof, "Analyzing the effects of free water modeling by deep learning on diffusion MRI structural connectivity estimates in glioma patients," *PLOS ONE*, vol. 15, no. 9, p. e0239475, Sep. 2020, doi: 10.1371/journal.pone.0239475.

11 Acknowledgments

At this point, I would like to warmly thank my supervisor, PD Dr. Benedikt Wiestler, for providing me such an interesting topic to research and for his continuous encouragement and support.
A special thank you also goes to my parents for always having faith in me.
Last but not least, thank you to all the colleagues, friends and family members who helped me completing this doctoral thesis.

I dedicate this work to my aunt who did not get the chance to receive the best neuroradiological treatment when she needed it.